



# Early Phases of Star Formation: Testing Chemical Tools

N. C. Martinez and S. Paron

CONICET-Universidad de Buenos Aires. Instituto de Astronomía y Física del Espacio, Ciudad Universitaria, (C1428EGA) Ciudad Autónoma de Buenos Aires, Argentina; [sparon@iafe.uba.ar](mailto:sparon@iafe.uba.ar)

Received 2023 August 24; revised 2023 October 7; accepted 2023 October 13; published 2023 December 12

## Abstract

Star-forming processes strongly influence the ISM chemistry. Nowadays, many high-quality databases are available at millimeter wavelengths. Using them, it is possible to carry out studies that review and deepen previous results. If these studies involve large samples of sources, it is preferred to use direct tools to study the molecular gas. With the aim of testing these tools such as the use of the HCN/HNC ratio as a thermometer, and the use of  $\text{H}^{13}\text{CO}^+$ ,  $\text{HC}_3\text{N}$ ,  $\text{N}_2\text{H}^+$  and  $\text{C}_2\text{H}$  as “chemical clocks,” we present a molecular line study toward 55 sources representing massive young stellar objects at different evolutionary stages: infrared dark clouds (IRDCs), high-mass protostellar objects (HMPOs), hot molecular cores (HMCs) and ultracompact H II regions. We found that the use of the HCN/HNC ratio as a universal thermometer in the ISM should be taken with care because the HCN optical depth is a big issue that can affect the method. Hence, this tool should be utilized only after a careful analysis of the HCN spectrum, checking that no line, neither the main nor the hyperfine ones, presents absorption features. We point out that the analysis of the emission of  $\text{H}^{13}\text{CO}^+$ ,  $\text{HC}_3\text{N}$ ,  $\text{N}_2\text{H}^+$  and  $\text{C}_2\text{H}$  could be useful to trace and distinguish regions among IRDCs, HMPOs and HMCs. The molecular line widths of these four species increase from the IRDC to the HMC stage, which can be a consequence of the gas dynamics related to the star-forming processes taking place in the molecular clumps. Our results not only contribute with more statistics, acting as a probe of such chemical tools, useful to obtain information in large samples of sources, but also complement previous works through the analysis of other types of sources.

*Key words:* stars: formation – ISM: molecules – ISM: clouds

## 1. Introduction

The sites in which the stars form are characterized by a rich and complex chemistry. The smallest gaseous fragments within a molecular cloud, known as hot molecular cores (HMCs), which are related to the formation of massive stars, are the chemically richest regions in the interstellar medium (ISM) (e.g., Herbst & van Dishoeck 2009; Bonfand et al. 2019). Molecules and chemistry are ubiquitous along all the stages that a forming star goes through, and moreover, the star-forming processes strongly influence the chemistry of such environments (Jørgensen et al. 2020). For instance, as material collapses and becomes ionized by the young massive stars and shocked by jets and outflows, temperature and density can change drastically, leading to the formation and destruction of molecular species. Thus, observing molecular lines and studying their emission and chemistry are important to shed light on the different stages of star formation and to characterize physical and chemical conditions.

To explore the star-forming processes in different environments, one should work with accurate values of the physical properties, such as the case of the kinetic temperature ( $T_K$ ). For example, calculating the excitation temperature ( $T_{\text{ex}}$ ) of carbon monoxide  $^{12}\text{C}^{16}\text{O}$ , the  $T_K$  of a molecular cloud can be roughly

estimated if it is assumed that there is a complete thermalization of the lines ( $T_{\text{ex}} = T_K$ ). Ammonia ( $\text{NH}_3$ ) has been found in different interstellar environments: from dark quiescent clouds, circumstellar envelopes, and early stages of high and low luminosity star formation to planetary atmospheres and external galaxies (Betz et al. 1979; Martin & Ho 1979; Ho & Barrett 1980; Rathborne et al. 2008; Takano et al. 2013; Bögner et al. 2022). Estimating the  $\text{NH}_3$  rotational temperature usually results in a reliable indicator of the kinetic temperature.

Hydrogen cyanide (HCN) and isocyanide (HNC) are two of the most simple molecules in the ISM, first detected almost fifty years ago (Snyder & Buhl 1971, 1972). These isomers have a linked chemistry, and differences in the spatial distributions in which they lie within a cloud can reflect the gas chemical conditions and the evolution of the star-forming regions (Schilke et al. 1992). Recently, Hacar et al. (2020) proposed the HCN-to-HNC integrated intensity ratio as a direct and efficient thermometer of the ISM with an optimal working range  $15\text{ K} \lesssim T_K \leq 40\text{ K}$ . The authors performed an analysis of such isomers throughout the Integral Shape Filament in Orion, deriving an empirical correlation between the HCN/HNC ratio and the kinetic temperature  $T_K$ . Based on the analysis of such correlation toward many dense molecular clumps from the

MALT90 survey, they proposed that the HCN/HNC thermometer can be extrapolated for the analysis of the ISM in general, particularly in star-forming sites, aiming to explore it toward different regions and sources along the ISM.

Molecular species that emerge and are destroyed during the birth of stars can be used to track the star-forming processes within molecular clumps and cores (Stephens et al. 2015; Urquhart et al. 2019). Comparisons between column densities and molecular abundance ratios that can be used to estimate the age and mark the evolutionary stages of star-forming regions are known as “chemical clocks.” As Sanhueza et al. (2012) pointed out, only molecules that exhibit differential abundances with time can be used to evaluate the evolutionary status of a star-forming region. In general, chemical clocks have been studied in depth in low-mass star-forming regions, but this effort has been less developed in the context of high-mass star-forming regions. As shown by Yu & Wang (2015), in the context of an analysis of chemical clocks it is important to not only study abundance ratios of such molecules, but also the integrated line intensities, the line widths, among other parameters. For instance, the molecular line widths ( $\Delta v^{\text{FWHM}}$ ) are related to the gas kinematics of the molecular clump interior, regarding turbulence, outflows and shocks among other processes (Sanhueza et al. 2012) which can give information about the evolutionary stage of a massive young stellar object (MYSO).

Some interesting molecular species for probing physical and chemical properties of star-forming regions are diazenylium ( $\text{N}_2\text{H}^+$ ) and ethynyl radical ( $\text{C}_2\text{H}$ ). Both molecules seem to be good tracers of dense gas in the early stages of the star-forming evolution (Beuther et al. 2008; Sanhueza et al. 2012, 2013),  $\text{N}_2\text{H}^+$  traces cold gas due to its resistance to depletion at low temperatures (Li et al. 2019), and the latter, additionally, can indicate the presence of a photodissociation region (PDR), where ultraviolet (UV) photons from young and hot massive stars irradiate acetylene to produce  $\text{C}_2\text{H}$  (Fuente et al. 1993; Nagy et al. 2015; García-Burillo et al. 2017).  $\text{HCO}^+$  and  $\text{H}^{13}\text{CO}^+$  (formylium species) are usually employed to investigate infall motions and outflow activity (Rawlings et al. 2004; Veena et al. 2018), and  $\text{HC}_3\text{N}$  is helpful to explore gas associated with HMCs (Bergin et al. 1996; Taniguchi et al. 2016; Duronea et al. 2019).

The mentioned molecules are among the brightest lines, and they were called molecular fingerprints in a study of a large sample of molecular clumps (Urquhart et al. 2019). As the authors pointed out, such molecules are able to trace a large range of physical conditions including cold and dense gas ( $\text{HNC}$ ,  $\text{H}^{13}\text{CO}^+$ ,  $\text{HCN}$ ,  $\text{HN}^{13}\text{C}$ ,  $\text{H}^{13}\text{CN}$ ), outflows ( $\text{HCO}^+$ ), early chemistry ( $\text{C}_2\text{H}$ ), and gas associated with protostars and young stellar objects (YSOs) ( $\text{HC}_3\text{N}$ , and cyclic molecules). Thus, the analysis of such molecules gives us a significant amount of scope to search for differences in the chemistry as a function of the evolutionary stage of the star formation taking place within molecular clumps. For instance, Yu & Wang

(2015) studied 31 extended green object (EGO) clumps with data from the MALT90 aiming to better understand the chemical processes that take place in the evolution of massive star formation. They classified the sources and made a molecular line study over 20 MYSOs and 11 H II regions. Through the comparison of integrated intensities, line widths and column densities, derived from the emission of  $\text{N}_2\text{H}^+$  and  $\text{C}_2\text{H}$  with those of the formylium ( $\text{H}^{13}\text{CO}^+$ ) and cyanoacetylene ( $\text{HC}_3\text{N}$ ), they suggested that  $\text{N}_2\text{H}^+$  and  $\text{C}_2\text{H}$  could act as efficient chemical clocks. They found that the  $\text{N}_2\text{H}^+$  and  $\text{C}_2\text{H}$  column densities decrease from MYSOs to H II regions, and the  $[\text{N}_2\text{H}^+]/[\text{H}^{13}\text{CO}^+]$  and  $[\text{C}_2\text{H}]/[\text{H}^{13}\text{CO}^+]$  abundance ratios also decrease with the evolutionary stage of the EGO clumps. In addition they ascertained that the velocity widths of  $\text{N}_2\text{H}^+$ ,  $\text{C}_2\text{H}$ ,  $\text{H}^{13}\text{CO}^+$  and  $\text{HC}_3\text{N}$  are comparable to each other in MYSOs, while in H II regions the velocity widths of  $\text{N}_2\text{H}^+$  and  $\text{C}_2\text{H}$  tend to be narrower than those of  $\text{H}^{13}\text{CO}^+$  and  $\text{HC}_3\text{N}$ .

Nowadays, many high-quality databases are available that were generated from observations obtained with the most important (sub)millimeter telescopes such as the IRAM 30 m Telescope and the Atacama Large Millimeter/submillimeter Array (ALMA), among others. For instance, using this kind of data, it is possible to carry out new chemical studies that, in turn, review and deepen previous results. If these studies involve large samples of sources, it is preferred to use direct tools to study and probe the molecular gas like what is presented in Hacar et al. (2020) and Yu & Wang (2015).

Infrared dark clouds (IRDCs) are massive, dense and cold clumps that may harbor budding stars, while high mass protostellar objects (HMPOs) are already protostars accreting material from their surroundings; at this stage, both temperature and density increase, but it is thought that at the beginning, they are chemically poor from an evolutionary point of view. HMCs are considered hotter sources where the chemistry is prolific as a consequence of embedded and evolved HMPOs (Giannetti et al. 2017) until they eventually reach the last stage here considered: ultracompact H II (UCHII) regions. The stars responsible for the UCHII regions have generally finished their accretion process and have begun to ionize the gas around them. All the processes involved in this evolutionary path impact the molecular gas that eventually can be investigated through the emission of molecular lines. It is important to highlight that the mentioned phases in the massive star formation may not have well-defined limits, and sometimes one determined source may have some physical conditions overlapping with those of another kind of source (e.g., Beuther et al. 2007; Gerner et al. 2014). Moreover, different kinds of sources may be embedded within the same molecular clump. Given this complex scenario, comparative studies with many sources are needed to analyze the involved physics and chemistry.

With the aim of testing the presented tools concerning the use of the HCN/HNC ratio as a thermometer (following the methodology published in Hacar et al. 2020), and the analysis

**Table 1**  
Analyzed Molecular Lines

Molecule	Transition	Rest Frequency (GHz)
$\text{H}^{13}\text{CO}^+$	1–0	86.7542
$\text{C}_2\text{H}^{\text{a}}$	1–0 $3/2-1/2$ $F=2-1$	87.3169
$\text{HCN}$	1–0 $F=1-1$	88.6304
	1–0 $F=2-1$	88.6318
	1–0 $F=0-1$	88.6339
$\text{HNC}$	1–0	90.6635
$\text{HC}_3\text{N}$	10–9	90.9790
$\text{N}_2\text{H}^{+\text{a}}$	1–0 $F_1=2-1$ $F=3-2$	93.1737

**Note.**

<sup>a</sup> Species with several observed hyperfine lines. Only the used line of each molecule is included in this work.

of  $\text{H}^{13}\text{CO}^+$ ,  $\text{HC}_3\text{N}$ ,  $\text{N}_2\text{H}^+$  and  $\text{C}_2\text{H}$  (following the methodology reported in Yu & Wang 2015), we present this study toward 55 sources representing MYSOs at different evolutionary stages as described above. After the presentation of the data and the analyzed sources (Section 2), the paper is structured as follows: a reporting of the results regarding each tested tool (Section 3), their respective discussion (Section 4) and a summary of the main results (Section 5).

## 2. Data and Analyzed Sources

We made use of the catalog “IRAM 30 m reduced spectra of 59 sources” J/A+A/563/A97 in the VizieR database<sup>1</sup> (Gerner et al. 2014), from which the molecular data were obtained and the sources were selected to perform our study. The particular molecular lines analyzed in our work are presented in Table 1. These data, obtained by Gerner et al. (2014), with the 30 m IRAM telescope, are single pointing spectra observed toward each source. The data used here correspond to the 86–94 GHz band, which have an angular and spectral resolution of  $29''$  and  $0.6 \text{ km s}^{-1}$  respectively, and typical  $1\sigma$  rms values of about  $0.03 \text{ K}$ .

The sources, classified as IRDCs, HMPOs, HMCs and UCHII, are presented in Table 2, where the coordinates and distances are included. The classification is based on the guidelines introduced by Beuther et al. (2007) and Zinnecker & Yorke (2007) according to the physical conditions of the evolutionary sequence in the formation of high-mass stars. IRDCs are sources that consist of cold and dense gas and dust that emit mainly at (sub) millimeter wavelengths. According to Gerner et al. (2014), the IRDCs of this sample consist of starless IRDCs as well as IRDCs already starting to harbor point sources at  $\mu\text{m}$ -wavelengths. HMPOs are sources hosting an actively accreting massive protostar(s), which shows an internal emission source at mid-infrared. HMCs are much warmer than HMPOs and can be

distinguished from a chemical point of view. At this stage, the central source(s) heats the surroundings evaporating molecular-rich ices. Finally, the UV radiation from the embedded massive protostar(s) ionizes the surrounding gas and gives rise to an UCHII region. Even though there might be overlaps among HMPO, HMC and even the UCHII stage, such classification was followed by Gerner et al. (2014) based on physical quantities, especially the temperature, which rises from IRDCs to HMPOs to UCHII regions, and based on the chemistry that can differentiate HMPOs (chemical poorer sources) from HMCs (molecularly richer chemistry sources). The sample includes 19 IRDCs, 20 HMPOs, 7 HMCs and 9 UCHII regions. In addition to the possible overlaps among the types of sources, it is possible that within the beam of the observational data lies more than one type of source. This is the case for HMC034.26, a region hosting several H II regions and a hot core. Thus, it is necessary to be careful with any analysis in relation to the evolutionary stages.

The quality of these IRAM data and the variety of sources in the sample included in such a catalog allow us to perform a new analysis of several molecular species in order to probe the molecular gas conditions and the chemistry related to IRDCs, HMPOs, HMCs and UCHII regions with the aim of probing chemical tools.

Additionally, we used infrared (IR) data to complement the information obtained from the molecular lines with the aim of probing, in these wavelengths, the activity of the star-forming regions. Data at the Ks band extracted from the UKIRT Infrared Deep Sky Survey (UKIDSS) (Lawrence et al. 2007) and IRAC-Spitzer  $4.5 \mu\text{m}$  data obtained from the Galactic Legacy Infrared Midplane Survey Extraordinaire (GLIMPSE) survey (Churchwell et al. 2009) were used.

## 3. Results

### 3.1. Infrared and Submillimeter Continuum Emission

Given that jets and outflows affect the star-forming regions’ chemistry, we looked for evidence of such processes by using IR data to have additional information on each source, besides its classification, to interpret and complement the molecular analysis. Data at the Ks band extracted from the UKIDSS were used to search for signs of jets (e.g., Paron et al. 2022) mainly in HMPOs, and also in HMCs and UCHII regions. IRAC-Spitzer  $4.5 \mu\text{m}$  data, obtained from the GLIMPSE survey, were employed to analyze whether the sources present extended  $4.5 \mu\text{m}$ , likely indicating outflow activity (e.g., Davis et al. 2007). Additionally, each source was checked if it is cataloged as an “EGO—likely MYSO outflow candidate” according to the catalog of Cyganowski et al. (2008).

In Table 2 (Cols. 6 and 7), we indicate the kind of emission at the Ks and  $4.5 \mu\text{m}$  bands observed within the beam size of the IRAM data centered at the position of each source. If one or several point sources appear within the IRAM beam, it is indicated as “points”; extended emission, suggesting the presence

<sup>1</sup> <http://cdsarc.u-strasbg.fr/viz-bin/qcat?J/A+A/563/A97>

**Table 2**  
Sample of Analyzed Sources

Name	R.A. (J2000)	Decl. (J2000)	Distance (kpc)	Type	Ks	4.5 $\mu\text{m}$	$F_{\text{peak}}(870 \mu\text{m})$ (Jy beam $^{-1}$ )
IRDC011.1	18 10 28.4	−19 22 34	3.60	IRDC	points	point	1.76
IRDC028.1	18 42 50.3	−04 03 20	4.80	IRDC	points	no	...
IRDC028.2	18 42 52.1	−03 59 54	4.80	IRDC	points	ext.	...
IRDC048.6	19 21 44.4	13 49 24	2.50	IRDC	points	no	...
IRDC079.1	20 32 22.0	40 20 10	1.00	IRDC	points	points	...
IRDC079.3	20 31 57.7	40 18 26	1.00	IRDC	no	points	...
IRDC18151	18 17 50.3	−12 07 54	3.00	IRDC	ext.	no	...
IRDC18182	18 21 15.0	−14 33 03	3.60	IRDC	points	points	0.99
IRDC18223	18 25 08.3	−12 45 27	3.70	IRDC	points	no	1.58
IRDC18306	18 33 32.1	−08 32 28	3.80	IRDC	points	no	0.68
IRDC18308	18 33 34.3	−08 38 42	4.90	IRDC	points	no	...
IRDC18310	18 33 39.5	−08 21 10	5.20	IRDC	points	no	0.92
IRDC18337	18 36 18.2	−07 41 00	4.00	IRDC	points	no	0.66
IRDC18385	18 41 17.4	−05 09 56	3.30	IRDC	points	no	0.53
IRDC18437	18 46 21.8	−02 12 21	7.30	IRDC	points	points	0.68
IRDC184.1	18 48 02.1	−01 53 56	6.40	IRDC	points	no	1.06
IRDC184.3	18 47 55.8	−01 53 34	6.00	IRDC	points	no	2.06
IRDC19175	19 19 50.7	14 01 23	1.10	IRDC	points	no	0.48
IRDC20081	20 10 13.0	27 28 18	0.70	IRDC	no	x	...
HMPO18089	18 11 51.6	−17 31 29	3.60	HMPO	ext.	points+ext.	9.25
HMPO18102	18 13 11.3	−18 00 03	2.70	HMPO	points	points	3.66
HMPO18151	18 17 58.1	−12 07 26	3.00	HMPO	jets	points+ext.	...
HMPO18182	18 21 09.2	−14 31 50	4.50	HMPO	diff.	points+ext. - EGO	5.66
HMPO18247	18 27 31.7	−11 45 56	6.70	HMPO	points	points+ext.	1.87
HMPO18264	18 29 14.6	−11 50 22	3.50	HMPO	ext.	ext. - EGO	7.43
HMPO18310	18 33 48.1	−08 23 50	5.20	HMPO	points	points	2.12
HMPO18488	18 51 25.6	00 04 07	5.40	HMPO	points	points	2.80
HMPO18517	18 54 14.4	04 41 40	2.90	HMPO	points	ext.	5.26
HMPO18566	18 59 10.1	04 12 14	6.70	HMPO	diff.	points+ext.	3.83
HMPO19217	19 23 58.8	16 57 44	10.50	HMPO	diff.	points+ext.	3.06
HMPO19410	19 43 11.0	23 44 10	2.10	HMPO	jets	ext.	5.31
HMPO20126	20 14 26.0	41 13 32	1.70	HMPO	jets	x	...
HMPO20216	20 23 23.8	41 17 40	1.70	HMPO	jets	ext.	...
HMPO20293	20 31 12.9	40 03 20	1.30	HMPO	diff.	ext.	...
HMPO22134	22 15 09.1	58 49 09	2.60	HMPO	diff.	ext.	...
HMPO23033	23 05 25.7	60 08 08	3.50	HMPO	x	x	...
HMPO23139	23 16 10.5	59 55 28	4.80	HMPO	x	x	...
HMPO23151	23 17 21.0	59 28 49	5.70	HMPO	x	x	...
HMPO23545	23 57 06.1	65 24 48	0.80	HMPO	x	x	...
HMC009.62	18 06 15.2	−20 31 37	5.70	HMC	diff.	ext.	12.48
HMC010.47	18 08 38.2	−19 51 50	5.80	HMC	points	points	35.01
HMC029.96	18 46 04.0	−02 39 21	7.40	HMC	points	ext.	12.01
HMC031.41	18 47 34.2	−01 12 45	7.90	HMC	points	ext.	61.68
HMC034.26	18 53 18.5	01 14 58	4.00	HMC	diff.	ext.	55.65
HMC045.47	19 14 25.7	11 09 26	6.00	HMC	ext.	ext. - EGO	5.49
HMC075.78	20 21 44.1	37 26 40	4.10	HMC	diff.+ext.	ext.	...
UCH005.89	18 00 30.4	−24 04 00	2.50	UCHII	ext.	ext.	25.73
UCH010.10	18 05 13.1	−19 50 35	4.40	UCHII	ext.	points	0.92
UCH010.30	18 08 55.8	−20 05 55	6.00	UCHII	diff.	ext. - EGO	7.67
UCH012.21	18 12 39.7	−18 24 20	13.50	UCHII	points	points	11.58
UCH013.87	18 14 35.8	−16 45 43	4.40	UCHII	diff.+ext.	ext.	5.52
UCH030.54	18 46 59.3	−02 07 24	6.10	UCHII	points	points+ext.	2.24
UCH035.20	19 01 46.4	01 13 25	3.20	UCHII	points+diff.	x	...
UCH045.12	19 13 27.8	10 53 37	6.90	UCHII	jets	ext.	7.58
UCH045.45	19 14 21.3	11 09 14	6.00	UCHII	ext.	ext.	3.90

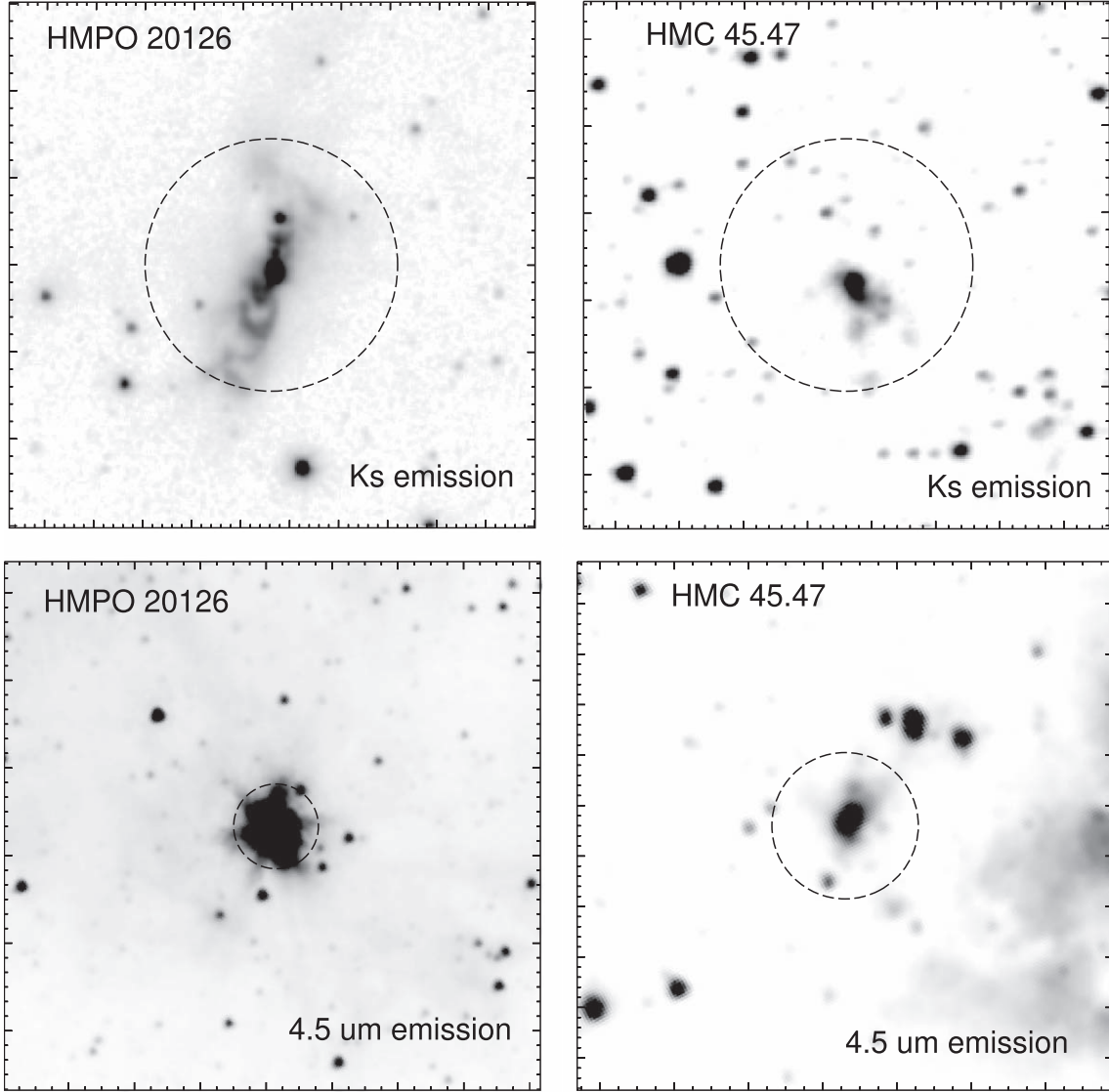


**Figure 1.** Near-IR Ks emission obtained from the UKIDSS database (top panels) and IRAC-Spitzer  $4.5 \mu\text{m}$  emission (bottom panels) toward HMPO 20126 and HMC 45.47, on the left and right respectively. In all cases, the dashed circle represents the position and the beam size ( $29''$ ) of the IRAM observations.

of jets and outflows, is signified as “ext.” and if this extended emission presents a jet-like morphology, it is stated as “jets.” Diffuse emission without any clear morphology is indicated as “diff.” While “no” means that there is no emission, an “x” indicates there are no data at the corresponding wavelength. In the case of the  $4.5 \mu\text{m}$  emission, if the source is cataloged as an “EGO—likely MYSO outflow candidate,” this is indicated with “EGO” in Col. 7. As an example, Figure 1 displays two sources in the Ks band: on the left HMC45.47 shows a jet-like feature and some extended emission at the  $4.5 \mu\text{m}$  band, while on the right HMC 45.47 appears with extended emission at both bands, and it is cataloged as an EGO.

Additionally, in Table 2 (Col. 8), we include the peak flux of the submillimeter emission obtained from the APEX Telescope Large Area Survey of the Galaxy (ATLASGAL) compact source catalog (Contreras et al. 2013; Urquhart et al. 2014) for sources that lie within the IRAM beam centered at the coordinates indicated in Cols. 2 and 3.

### 3.2. HCN/HNC Ratio and $T_K$

Following the same procedure as done by Hacar et al. (2020) when they test the HCN/HNC kinetic temperature in a large sample of dense molecular clumps extracted from the MALT90 survey (see their Section 4.4), we derived the  $T_K$  for each source



of the sample presented here. The correlation to derive  $T_K$  proposed by the authors is as follows: if the integrated intensity ratio of the isomers HCN and HNC (hereafter  $I(\text{HCN})/I(\text{HNC})$ ) is  $\leq 4$ ,  $T_K$  is estimated as  $T_K = 10 \times I(\text{HCN})/I(\text{HNC})$ ; and if  $I(\text{HCN})/I(\text{HNC}) > 4$ ,  $T_K = 3 \times (I(\text{HCN})/I(\text{HNC}) - 4) + 40$  is used. As done by Hacar et al. (2020), we integrated the HCN ( $J = 1-0$ ), including all hyperfine components and HNC ( $J = 1-0$ ) over a given velocity interval (in Appendix we include some spectra indicating the integrated area in both isomers). The obtained integrated emission values, and the respective ratios, are presented in Table 3 (Cols. 2, 3 and 4, respectively), and the obtained kinetic temperatures following the mentioned relations are presented in Table 4. Typical errors in  $I(\text{HCN})$  and  $I(\text{HNC})$  are about 0.2 and 0.1 K km s<sup>-1</sup>, respectively, which yield errors between 1 and 5%, and in some cases at most 10%, in the  $T_K$ . From now on, the obtained errors in the measured and derived parameters appear as bars in the figures, and for a better display, we do not include them in the tables.

In the further analysis and comparisons, following Hacar et al. (2020), we do not consider values of kinetic temperatures obtained from the HCN/HNC ratio (hereafter  $T_K(\text{HCN}/\text{HNC})$ ) lower than 15 K. These values are due to  $I(\text{HCN})/I(\text{HNC})$  ratios close to the unity, which according to the authors, the uncertainties in the method grow for such cases, likely due to the combination of excitation and opacity effects. In Section 4.1.1, based on the inspection of the HCN and HNC spectra of sources for which  $T_K(\text{HCN}/\text{HNC}) < 15$  K, we discuss this issue.

In order to compare the  $T_K(\text{HCN}/\text{HNC})$ , we sought the dust temperature of each source. Dust temperature ( $T_{\text{dust}}$ ) values were obtained from the maps<sup>2</sup> generated by the point process mapping (PPMAP) algorithm (Marsh et al. 2015) done to the Herschel infrared Galactic Plane Survey (Hi-GAL) maps in the wavelength range 70–500  $\mu\text{m}$  (Marsh et al. 2017).  $T_{\text{dust}}$  values are included in Table 4, and they represent average values on the dust temperature map over the IRAM beam size centered at the source position. Additionally, we also compared with the ammonia kinetic temperature ( $T_K(\text{NH}_3)$ ) derived by Urquhart et al. (2011) in several sources of the sample analyzed here that are contained in the Red MSX Source survey (Hoare et al. 2005; Mottram et al. 2006; Urquhart et al. 2008).

Figure 2 exhibits the comparisons between  $T_K(\text{NH}_3)$  and  $T_{\text{dust}}$  (upper panel),  $T_{\text{dust}}$  and  $T_K(\text{HCN}/\text{HNC})$  (middle panel), and  $T_K(\text{NH}_3)$  and  $T_K(\text{HCN}/\text{HNC})$  (bottom panel). Table 5 presents the average temperature values with their errors. As mentioned above, sources with values  $T_K(\text{HCN}/\text{HNC}) < 15$  K were not considered, either in the figures or in the calculated average.

### 3.3. Molecules as “Chemical Clocks”?

Following Yu & Wang (2015), we performed a similar analysis using the HNC, C<sub>2</sub>H, HC<sub>3</sub>N, H<sup>13</sup>CO<sup>+</sup> and N<sub>2</sub>H<sup>+</sup> emissions measured toward the sources presented in Table 2. This is: (1) we compared the molecular emissions with the flux at the submillimeter continuum, (2) we analyzed the line widths of the C<sub>2</sub>H, HC<sub>3</sub>N, H<sup>13</sup>CO<sup>+</sup> and N<sub>2</sub>H<sup>+</sup>, and (3) we analyzed the column densities (extracted from Gerner et al. 2014) of C<sub>2</sub>H and N<sub>2</sub>H<sup>+</sup> by comparing with that of the H<sup>13</sup>CO<sup>+</sup>.

Figure 3 displays the integrated intensities of HNC, C<sub>2</sub>H, HC<sub>3</sub>N and N<sub>2</sub>H<sup>+</sup> (presented in Table 3) versus the 870  $\mu\text{m}$  peak flux obtained from the ATLASGAL compact source catalog (presented in Col. 8 in Table 2).

We fitted the line emission of C<sub>2</sub>H, N<sub>2</sub>H<sup>+</sup>, H<sup>13</sup>CO<sup>+</sup> and HC<sub>3</sub>N with Gaussian functions to obtain the full width at half maximum (FWHM) line widths ( $\Delta\nu$ ) in each source (in Appendix we include some spectra showing the Gaussian fittings). In the case of the C<sub>2</sub>H and N<sub>2</sub>H<sup>+</sup>, which have hyperfine components, the fitting was done with multiple Gaussian functions, and the  $\Delta\nu$  values used in this analysis correspond to the main components. These values are presented in Table 6. The absence of values in some sources is due to a lack of emission or that the hyperfine components are completely blended with the main component. Table 7 expresses the average line widths for each kind of source, and with the aim of analyzing their behavior, following the analysis reported in Yu & Wang (2015), we present plots that display relations among the measured  $\Delta\nu$  in Figure 4.

From Gerner et al. (2014) we obtained the column densities of C<sub>2</sub>H, N<sub>2</sub>H<sup>+</sup> and H<sup>13</sup>CO<sup>+</sup> for each source. We used the column densities obtained as “iteration 1” according to the model used by the authors, which are the values derived with the mean temperatures from the best-fit models of “iteration 0.” Values indicated as upper limits are not included in our analysis. Figure 5 displays the column densities of C<sub>2</sub>H and N<sub>2</sub>H<sup>+</sup> versus the H<sup>13</sup>CO<sup>+</sup> column density. Error bars are not included, given that the authors did not inform them in their work. Finally, Figure 6 depicts the relative abundance of  $[\text{C}_2\text{H}]/[\text{H}^{13}\text{CO}^+]$  versus  $[\text{N}_2\text{H}^+]/[\text{H}^{13}\text{CO}^+]$ .

## 4. Discussion

Unlike low-mass stars, the formation of high-mass stars is not yet fully understood, and different scenarios have been proposed (see e.g., Tan et al. 2014; Motte et al. 2018). Probing the chemical conditions of high-mass star-forming regions at different evolutionary stages is an important issue to advance in knowledge on the formation of this kind of star, and to explore such chemical conditions, it is necessary to use efficient tools.

In this context, we decided to test the HCN/HNC ratio as a thermometer of the gas, as well as the use of the emission of H<sup>13</sup>CO<sup>+</sup>, HC<sub>3</sub>N, N<sub>2</sub>H<sup>+</sup> and C<sub>2</sub>H as “chemical clocks.” The obtained results from each study are discussed in what follows.

<sup>2</sup> <http://www.astro.cardiff.ac.uk/research/ViaLactea/>

**Table 3**  
Integrated line Intensities (Units in K km s<sup>-1</sup>) and the Ratio between HCN and HNC

Source	$I(\text{HCN})$	$I(\text{HNC})$	$I(\text{HCN}/\text{HNC})$	$I(\text{N}_2\text{H}^+)^a$	$I(\text{HC}_3\text{N})$	$I(\text{H}^{13}\text{CO}^+)$	$I(\text{C}_2\text{H})^b$
IRDC011.1	6.83	7.27	0.94	8.74	2.29	2.01	1.52
IRDC028.1	16.70	12.50	1.34	10.50	3.49	1.83	2.02
IRDC028.2	8.71	8.34	1.04	11.20	7.62	2.46	3.14
IRDC048.6	3.36	2.80	1.20	2.84	0.22	0.69	0.25
IRDC079.1	7.96	4.86	1.64	6.11	0.69	2.01	1.55
IRDC079.3	6.40	5.50	1.16	5.59	0.97	2.08	1.94
IRDC18151	49.10	19.50	2.52	13.90	2.42	2.63	5.12
IRDC18182	6.03	3.93	1.54	4.63	0.74	0.79	1.32
IRDC18223	18.90	11.90	1.59	13.20	2.04	2.60	2.11
IRDC18306	1.28	2.45	0.52	2.57	0.40	0.58	0.66
IRDC18308	14.30	8.68	1.65	6.51	1.25	0.85	1.34
IRDC18310	2.59	5.15	0.50	9.38	1.76	1.02	0.73
IRDC18337	1.08	1.80	0.60	5.94	...	0.95	0.89
IRDC18385	6.51	3.27	1.99	4.79	1.08	0.82	1.03
IRDC18437	6.93	4.24	1.63	...	0.34	0.40	1.07
IRDC184.1	0.60	1.29	0.47	4.78	0.45	0.60	1.11
IRDC184.3	11.50	12.80	0.90	...	1.86	...	2.51
IRDC19175	2.46	2.54	0.97	1.76	0.18	0.47	0.52
IRDC20081	6.62	2.96	2.24	2.11	...	1.02	1.20
HMPO18089	10.40	8.57	1.21	17.90	9.75	4.80	5.23
HMPO18102	22.60	19.90	1.14	19.70	5.71	2.97	2.87
HMPO18151	49.10	20.00	2.46	11.40	4.43	3.50	5.18
HMPO18182	34.00	15.20	2.24	14.90	5.55	3.78	4.28
HMPO18247	10.60	8.64	1.23	8.29	1.13	1.24	1.83
HMPO18264	74.10	26.90	2.76	25.50	6.55	5.08	7.14
HMPO18310	8.60	8.52	1.01	11.20	2.41	2.20	3.19
HMPO18488	7.31	10.20	0.72	13.20	3.88	2.59	3.93
HMPO18517	48.20	20.50	2.35	14.00	5.03	4.85	6.66
HMPO18566	11.20	11.60	0.97	12.50	5.72	3.02	2.95
HMPO19217	18.30	9.98	1.83	11.60	3.22	3.20	3.10
HMPO19410	38.70	18.40	2.10	22.50	5.70	3.17	6.11
HMPO20126	55.70	24.90	2.24	15.90	5.68	3.65	6.63
HMPO20216	15.90	7.74	2.05	3.34	0.98	1.31	2.56
HMPO20293	29.70	19.20	1.55	21.30	4.56	2.55	5.22
HMPO22134	13.30	4.87	2.73	2.51	1.82	1.09	3.07
HMPO23033	35.70	17.00	2.10	12.80	3.99	3.26	5.97
HMPO23139	31.10	9.69	3.21	6.91	2.72	1.49	4.13
HMPO23151	14.50	3.38	4.29	...	0.35	0.43	2.36
HMPO23545	6.79	2.14	3.18	0.39	0.14	0.74	1.28
HMC009.62	45.10	38.70	1.17	19.70	15.30	8.91	11.90
HMC010.47	110.30	51.20	2.15	...	24.50	9.69	12.60
HMC029.96	49.20	28.90	1.70	10.50	11.20	6.10	6.97
HMC031.41	19.70	12.70	1.55	...	15.40	2.72	6.14
HMC034.26	24.70	42.70	0.58	...	27.20	14.50	9.90
HMC045.47	23.20	20.90	1.11	22.50	6.72	5.75	5.06
HMC075.78	33.90	20.40	1.66	11.00	6.78	4.51	6.36
UCH005.89	130.50	91.70	1.42	35.00	57.60	15.40	21.8
UCH010.10	4.48	2.23	2.01	...	...	...	...
UCH010.30	95.10	53.30	1.78	18.50	19.00	6.49	15.10
UCH012.21	13.60	24.10	0.56	...	10.50	4.30	7.42
UCH013.87	31.30	14.00	2.24	7.67	4.35	3.59	6.90
UCH030.54	21.20	9.92	2.14	2.67	1.03	0.93	2.61
UCH035.20	26.40	14.40	1.83	7.27	3.13	2.46	3.90
UCH045.12	43.40	19.00	2.28	2.97	2.34	2.99	5.42
UCH045.45	22.10	10.30	2.15	4.06	1.64	1.28	2.96

**Notes.**

<sup>a</sup> Integrated line intensity of the N<sub>2</sub>H<sup>+</sup> main component (1–0  $F_1 = 2-1$   $F = 3-2$ ).

<sup>b</sup> Integrated line intensity of the C<sub>2</sub>H main component (1–0  $3/2-1/2$   $F = 2-1$ ).

**Table 4**  
Kinetic Temperatures Obtained from the Different Methods (Units in K)

Source	$T_K(\text{HCN}/\text{HNC})$	$T_{\text{dust}}$	$T_K(\text{NH}_3)$	Source	$T_K(\text{HCN}/\text{HNC})$	$T_{\text{dust}}$	$T_K(\text{NH}_3)$
IRDC011.1	9.4	18.0	...	HMPO18566	9.7	22.8	19.9
IRDC028.1	13.4	17.0	...	HMPO19217	18.3	23.6	27.5
IRDC028.2	10.4	17.0	...	HMPO19410	21.0	23.6	22.1
IRDC048.6	12.0	19.0	...	HMPO20126	22.4	...	23.1
IRDC079.1	16.4	15.0	15.3	HMPO20216	20.5	...	19.2
IRDC079.3	11.6	14.0	...	HMPO20293	15.5	20.2	20.1
IRDC18151	25.2	...	...	HMPO22134	27.3	24.5	20.9
IRDC18182	15.3	20.0	...	HMPO23033	21.0	...	18.5
IRDC18223	15.9	18.0	...	HMPO23139	32.1	...	27.7
IRDC18306	5.2	19.0	...	HMPO23151	40.9	...	...
IRDC18308	16.5	19.0	...	HMPO23545	31.8	...	...
IRDC18310	5.0	20.0	...				
IRDC18337	6.0	20.0	...	HMC009.62	11.7	25.1	...
IRDC18385	19.9	20.0	...	HMC010.47	21.5	23.2	...
IRDC18437	16.3	20.0	...	HMC029.96	17	26.7	33.0
IRDC184.1	4.7	20.0	...	HMC031.41	15.5	...	20.3
IRDC184.3	9.0	19.0	...	HMC034.26	5.8	28.4	...
IRDC19175	9.7	20.0	...	HMC045.47	11.1	25.1	26.4
IRDC20081	22.4	...	...	HMC075.78	16.6	27.2	...
HMPO18089	12.1	23.4	23.0	UCH005.89	14.2	26.8	...
HMPO18102	11.4	17.8	...	UCH010.10	20.1	21.8	...
HMPO18151	24.6	...	23.8	UCH010.30	17.8	26	...
HMPO18182	22.4	21.5	...	UCH012.21	5.6	23.1	...
HMPO18247	12.3	22.4	20.1	UCH013.87	22.4	26.9	...
HMPO18264	27.5	20	22.2	UCH030.54	21.4	25.5	32.6
HMPO18310	10.1	20	...	UCH035.20	18.3	...	26.1
HMPO18488	7.2	22	18.6	UCH045.12	22.8	31.3	...
HMPO18517	23.5	...	...	UCH045.45	21.5	29.3	25.4

#### 4.1. Testing the use of HCN/HNC Ratio as a Thermometer

Employing simple molecules, ubiquitous in star-forming regions, to derive their physical parameters is a helpful strategy for methodically analyzing many regions and avoiding complex calculations. In this context, we use the HCN/HNC intensity ratio formulation proposed recently by Hacar et al. (2020) to estimate the kinetic temperature ( $T_K(\text{HCN}/\text{HNC})$ ). As done by the authors, we probed them through comparisons with dust temperature ( $T_{\text{dust}}$ ) and  $T_K$  obtained from the ammonia emission ( $T_K(\text{NH}_3)$ ), when those parameters were available toward the sources of the analyzed sample. It is worth noting that the useful kinetic temperature range derived from the ammonia is between 15 and 40 K (Ho & Townes 1983; Urquhart et al. 2011), in coincidence with the valid range indicated for  $T_K(\text{HCN}/\text{HNC})$ .

Despite the limited amount of sources satisfying that the obtained  $T_K$  from the HCN/HNC ratio is  $>15$  K with measured values of  $T_{\text{dust}}$  and  $T_K(\text{NH}_3)$  (see Table 4), some conclusion can be extracted. Also, from the sources with  $T_K(\text{HCN}/\text{HNC}) < 15$  K or lower than expected, we can obtain important conclusions about this tool.

The comparison between  $T_{\text{dust}}$  and  $T_K(\text{NH}_3)$  (see upper panel of Figure 2) indicates that, within a range of 0–5 K of difference between both temperatures, the molecular gas and the dust could be considered that are thermally coupled, allowing us to suggest that in general this property could be extrapolated to the whole sample. This supports that the comparison between  $T_K(\text{HCN}/\text{HNC})$ , which is obtained from the gas emission, and the  $T_{\text{dust}}$  can be made.

Valid kinetic temperature values obtained following the HCN/HNC ratio (i.e.,  $>15$  K) seem to be more accurate for IRDCs and HMPOs than for HMCs and UCHII regions. By analyzing the average values (see Table 5),  $T_K$  obtained from the dust and ammonia emissions increases from IRDCs to UCHII regions as expected, but  $T_K(\text{HCN}/\text{HNC})$  increases only from IRDCs to HMPOs, and then it decreases in HMCs and UCHII regions. This suggests that in such sources, using the HCN–HNC tool to derive  $T_K$  can be not appropriate, and it may underestimate the actual temperature value.

Hacar et al. (2020) calculated the  $T_K(\text{HCN}/\text{HNC})$  toward a large sample of dense clumps extracted from the MALT90 survey (Foster et al. 2011; Jackson et al. 2013), and compared them with the  $T_{\text{dust}}$  measurements derived by Guzmán et al. (2015). At this



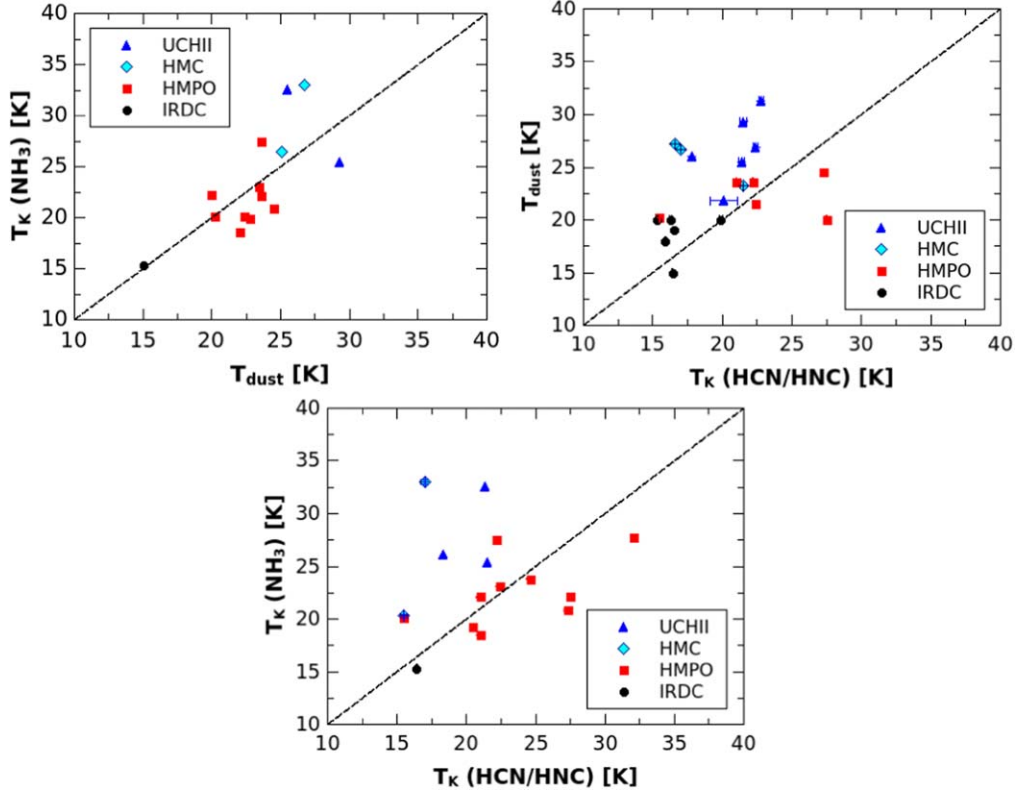


**Figure 2.** Top-left: Kinetic temperature of ammonia derived from transitions  $(J, K) = (2, 2) - (1, 1)$  versus dust temperature. Top-right: Dust temperature obtained from PPMAP output produced with the Hi-GAL maps (Marsh et al. 2017) versus kinetic temperature derived from the HCN–HNC integrated intensity ratio. Bottom: Kinetic temperature obtained from the ammonia versus kinetic temperature derived from the HCN–HNC integrated intensity ratio. The dashed black line, in all cases, indicates unity. Error bars in the  $T_K(\text{HCN}/\text{HNC})$  are displayed, and most of them are represented by the symbol size.

point, they stated that the comparison between  $T_K$  and  $T_{\text{dust}}$  should be done with caution given the fact that the beam resolution of the MALT90 targets and the measurement sensitivity within this beam do not allow resolving the temperature of individual clumps. Anyway, they pointed out that a correspondence between both temperatures prevails despite the mentioned observational caveats. However, they do not discuss the optical depth issue in the MALT90 sample as they did for their Orion results. This is an important matter to be considered, mainly when we work with a sample of different kinds of sources. As Hacar et al. (2020) mention, the increase of the HCN  $J = 1-0$  line opacity, while the HNC  $J = 1-0$  line likely remains optically thin, would reduce the HCN/HNC ratio, decreasing the values of  $T_K(\text{HCN}/\text{HNC})$ . This phenomenon could be occurring in the sources with  $T_K(\text{HCN}/\text{HNC}) < 15$  K (see Section 4.1.1) and in some other sources that, although the  $T_K$  obtained from the HCN–HNC tool is greater than 15 K, their values are well below the temperatures obtained from the dust and/or ammonia (about 10 K of difference). This is the case of HMCs and UCHII regions in our sample, in which, in general, it is observed that the HCN

**Table 5**  
Calculated Average Temperatures (Units in K)

Source	$T_{\text{dust}}$	$T_K(\text{NH}_3)$	$T_K(\text{HCN}/\text{HNC})$
IRDC	$18.5 \pm 0.4$	$15.3^a$	$18.5 \pm 1.2$
HMPO	$21.8 \pm 0.6$	$22.2 \pm 0.8$	$24.9 \pm 1.7$
HMC	$26.0 \pm 0.6$	$26.6 \pm 3.7$	$16.3 \pm 1.6$
UCHII	$26.3 \pm 1.1$	$28.0 \pm 2.3$	$19.8 \pm 1.0$

**Note.**

<sup>a</sup> Value obtained from a single source.

hyperfine line  $F = 1-1$  appears absorbed, indicating high optical depths (for an example, see Figure A5).

#### 4.1.1. Sources with $T_K(\text{HCN}/\text{HNC}) < 15$ K

In our sample, there are several sources such that the HCN/HNC ratio yields kinetic temperatures lower than 15 K, which were neither included in the analysis nor the comparisons with  $T_{\text{dust}}$  and  $T_K(\text{NH}_3)$  performed above. These sources have  $I(\text{HCN})/I(\text{HNC})$  ratios close to unity or even lower than one, which according to Hacar et al. (2020), in those cases, the

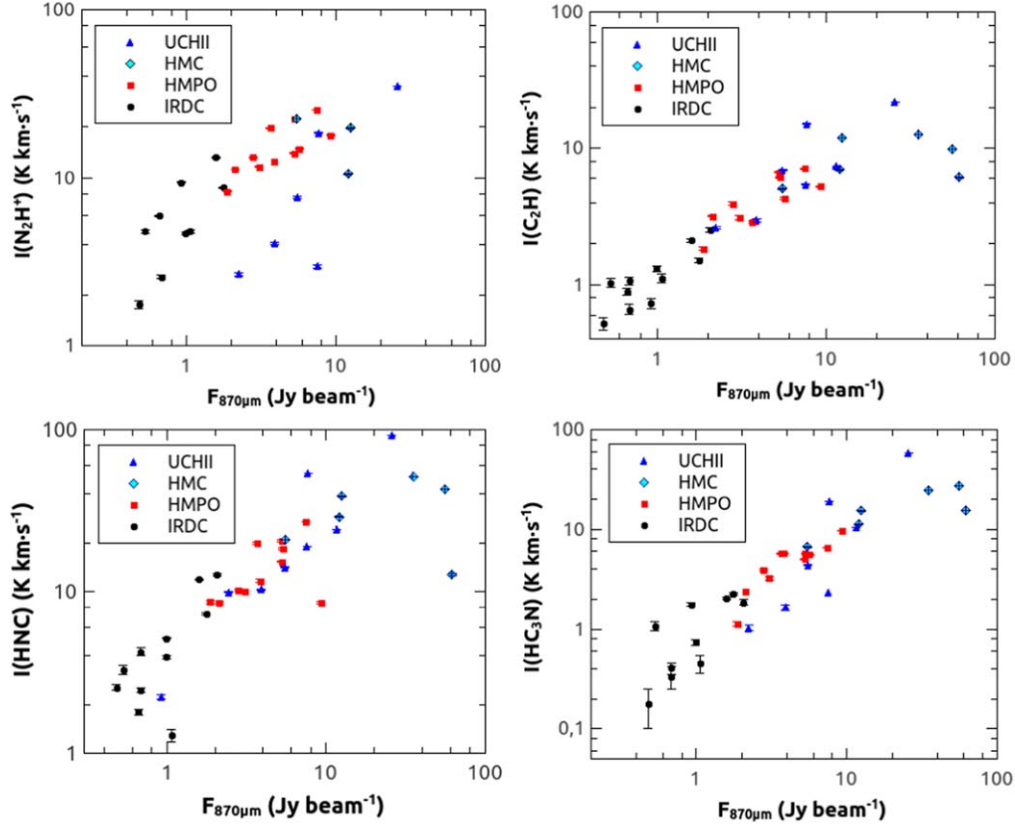


**Figure 3.** Plots of the integrated line emission versus the 870  $\mu\text{m}$  peak flux. Top panels display  $\text{N}_2\text{H}^+$  (main component, left) and  $\text{C}_2\text{H}$  (main component, right). Bottom panels feature: HNC (left) and  $\text{HC}_3\text{N}$  (right). Error bars in the y-axis represent the formal error in the integration of the line emissions.

uncertainties seem to increase, likely due to the combination of excitation and opacity effects. The percentages of sources with this issue are: 58%, 30%, 28% and 11% for IRDCs, HMPOs, HMCs and UCHII regions, respectively, suggesting that may be a condition that is more pronounced at earlier stages.

Taking into consideration the HCN hyperfine line anomalies (Walmsley et al. 1982; Loughnane et al. 2012), which prevent obtaining reliable values of HCN opacities, we carefully analyzed each HCN and HNC spectrum to look for signatures of high optical depths. We found that the HCN spectra of sources with  $T_K(\text{HCN}/\text{HNC}) < 15$  K have pronounced saturation and/or self-absorption features in some cases at both the main component and hyperfine lines (see Figure 7 for an example), and in other cases in the hyperfine line  $F=1-1$ . In the case of the HNC, we did not find such spectral features.

We point out that the use of the HCN/HNC ratio as a universal thermometer in the ISM should be taken with care. We suggest that such a thermometer could be used only in some IRDCs and HMPOs (when the derived kinetic temperature is not lower than 15 K; see Section 4.1.1) and in more evolved regions, for instance, HMCs and UCHII regions, this tool underestimates the temperature. Thus, we conclude that the

HCN–HNC tool as a kinetic temperature estimator should be used only after a careful analysis of the HCN spectrum, checking that no line, either the main or the hyperfine ones, presents absorption features; otherwise, it is not an useful tool for calculating kinetic temperatures.

#### 4.2. An Exploration of Molecules as “Chemical Clocks”

Molecular species such as HNC, HCN,  $\text{H}^{13}\text{CO}^+$ ,  $\text{C}_2\text{H}$  and  $\text{HC}_3\text{N}$  are relatively easy to be observed and they give us a significant amount of scope to search for differences in the chemistry as a function of the evolutionary stage in massive star-forming regions (Sanhueza et al. 2012; Yu & Wang 2015; Urquhart et al. 2019). After a similar analysis as presented by Yu & Wang (2015) performed on our sample of massive star-forming regions, in what follows we discuss our results.

First, from the comparison between the molecular integrated intensities and the 870  $\mu\text{m}$  peak flux (see Figure 3), we found that, in general, the integrated intensities of  $\text{N}_2\text{H}^+$ ,  $\text{C}_2\text{H}$ , HNC and  $\text{HC}_3\text{N}$  increase with the submillimeter peak flux. In the case of IRDCs, HMPOs and HMCs, this increment correlates with the evolutionary stage of the sources, i.e., the position of each kind of source in the plots seems to be sectorized. UCHII

**Table 6**  
FWHM  $\Delta v$  from Gaussian Fittings (Units in  $\text{km s}^{-1}$ )

Source	$\Delta v(\text{N}_2\text{H}^+)^a$	$\Delta v(\text{HC}_3\text{N})$	$\Delta v(\text{H}^{13}\text{CO}^+)$	$\Delta v(\text{C}_2\text{H})^b$
IRDC011.1	3.03	2.10	2.11	2.11
IRDC028.1	3.39	2.87	2.69	2.57
IRDC028.2	2.75	3.62	3.22	3.53
IRDC048.6	2.27	1.31	1.52	1.11
IRDC079.1	2.30	1.01	1.68	1.79
IRDC079.3	2.54	1.20	1.68	1.72
IRDC18151	3.08	3.28	2.53	3.85
IRDC18182	2.76	2.17	1.61	2.45
IRDC18223	3.41	2.86	2.78	2.87
IRDC18306	2.84	2.43	1.74	2.03
IRDC18308	3.82	2.68	2.17	3.00
IRDC18310	3.46	2.97	2.11	2.61
IRDC18337	3.10	...	1.84	2.85
IRDC18385	2.67	3.17	1.30	1.96
IRDC18437	...	1.74	1.52	1.88
IRDC184.1	2.88	2.32	2.53	2.90
IRDC184.3	...	2.52	...	4.60
IRDC19175	2.82	...	1.95	1.72
IRDC20081	1.91	...	1.16	1.56
HMPO18089	3.39	3.60	3.54	3.47
HMPO18102	5.00	3.67	3.65	3.49
HMPO18151	2.50	1.90	2.16	2.26
HMPO18182	3.55	3.05	3.02	3.29
HMPO18247	3.15	2.43	2.52	2.66
HMPO18264	3.31	3.14	2.53	3.01
HMPO18310	3.14	1.88	2.33	2.23
HMPO18488	3.48	3.20	3.15	4.61
HMPO18517	3.16	2.86	2.52	2.97
HMPO18566	3.94	3.62	3.73	4.20
HMPO19217	4.41	4.25	3.99	3.75
HMPO19410	2.50	1.85	1.80	1.99
HMPO20126	2.54	2.41	2.38	2.34
HMPO20216	2.20	1.33	1.37	1.82
HMPO20293	2.58	1.88	1.94	2.03
HMPO22134	2.17	1.25	1.69	1.84
HMPO23033	3.00	2.35	2.52	2.58
HMPO23139	2.83	2.50	2.48	2.92
HMPO23151	...	1.81	2.24	2.42
HMPO23545	2.05	1.34	2.34	1.80
HMC009.62	4.41	4.96	4.02	4.14
HMC010.47	...	7.48	7.06	6.95
HMC029.96	3.09	3.52	2.72	3.27
HMC031.41	...	5.99	4.90	7.03
HMC034.26	...	6.33	4.71	3.46
HMC045.47	4.41	3.93	4.31	4.33
HMC075.78	3.90	3.00	3.54	4.36
UCH005.89	3.50	3.94	3.64	3.33
UCH010.10	...	...	...	...
UCH010.30	4.58	4.54	4.35	6.26
UCH012.21	...	7.87	5.94	6.14
UCH013.87	3.14	2.46	2.53	2.94
UCH030.54	3.59	2.42	2.55	3.18
UCH035.20	3.29	3.23	3.32	2.73
UCH045.12	4.05	3.98	3.39	4.00
UCH045.45	3.20	3.92	3.41	4.70

**Notes.**<sup>a</sup>  $\Delta v$  of the  $\text{N}_2\text{H}^+$  main component ( $1-0 F_1 = 2-1 F = 3-2$ ).<sup>b</sup>  $\Delta v$  of the  $\text{C}_2\text{H}$  main component ( $1-0 3/2-1/2 F = 2-1$ ).

**Table 7**  
Average values of the Molecular Line Widths (Units in  $\text{km s}^{-1}$ )

Source	$\Delta v(\text{N}_2\text{H}^+)$	$\Delta v(\text{HC}_3\text{N})$	$\Delta v(\text{H}^{13}\text{CO}^+)$	$\Delta v(\text{C}_2\text{H})$
IRDC	$2.88 \pm 0.11$	$2.39 \pm 0.19$	$2.00 \pm 0.13$	$2.47 \pm 0.20$
HMPO	$3.09 \pm 0.17$	$2.51 \pm 0.19$	$2.59 \pm 0.16$	$2.78 \pm 0.18$
HMC	$3.95 \pm 0.31$	$5.02 \pm 0.62$	$4.46 \pm 0.51$	$4.79 \pm 0.58$
UCHII	$3.62 \pm 0.20$	$4.04 \pm 0.60$	$3.64 \pm 0.38$	$4.19 \pm 0.49$

regions show the same trend, but their points are overlapped with those of the other sources in all cases except for the  $\text{N}_2\text{H}^+$  case. Yu & Wang (2015) found that the  $\text{N}_2\text{H}^+$  integrated intensities of HII regions tend to be lower than those for MYSOs. This behavior seems to occur with the UCHII regions of our sample in comparison with the other sources, suggesting that the destruction path due to electronic recombination, where  $\text{N}_2\text{H}^+$  is destroyed by free electrons from the surroundings (Vigren et al. 2012), could be ongoing in the UCHII regions. This result complements what was presented by Yu & Wang (2015) with sources at earlier stages, and suggests that the relation between the molecular integrated intensities and the  $870 \mu\text{m}$  peak flux could be useful to distinguish regions among IRDCs, HMPOs and HMCs.

The comparisons between the column densities obtained from Gerner et al. (2014) also show an interesting trend regarding the evolutionary stage of the sources. Yu & Wang (2015) stated, based on astrochemical models (e.g., Bergin et al. 1997; Nomura & Millar 2004), that the  $\text{H}^{13}\text{CO}^+$  column density reflects the amount of  $\text{H}_2$  density in a clump because its abundance seems to not vary much with time. In line with their work, we compared  $N(\text{C}_2\text{H})$  and  $N(\text{N}_2\text{H}^+)$  with  $N(\text{H}^{13}\text{CO}^+)$  (see Figure 5). The  $N(\text{H}^{13}\text{CO}^+)$  values of our sample range in a wider interval of values (from some  $10^{12} \text{ cm}^{-2}$  for IRDCs to values close to  $10^{14} \text{ cm}^{-2}$  for HMCs) than the  $N(\text{H}^{13}\text{CO}^+)$  presented by Yu & Wang (2015). An increase in the  $N(\text{C}_2\text{H})$  and  $N(\text{N}_2\text{H}^+)$  with the  $N(\text{H}^{13}\text{CO}^+)$  is observed. In the case of  $N(\text{C}_2\text{H})$  versus  $N(\text{H}^{13}\text{CO}^+)$  relation, such an increment also presents a conspicuous correlation with the evolutionary stage from IRDCs to HMCs in which the positions of each kind of source are sectorized in the plot. In the UCHII regions, both column densities have similar values compared with those of HMCs and the largest ones of HMPOs. A similar behavior, with larger dispersion, is observed in the comparison between  $N(\text{N}_2\text{H}^+)$  versus  $N(\text{H}^{13}\text{CO}^+)$ . The  $\text{N}_2\text{H}^+$  and  $\text{H}^{13}\text{CO}^+$  column density increment from IRDCs to HMCs could be explained by their progressive formation through the  $\text{H}_3^+$  mechanisms ( $\text{H}_3^+ + ^{13}\text{CO} \rightarrow \text{H}^{13}\text{CO}^+ + \text{H}_2$ , and  $\text{H}_3^+ + \text{N}_2 \rightarrow \text{N}_2\text{H}^+ + \text{H}_2$ ; Jørgensen et al. 2004). Then, the brake on the constant increment in the column density values in the UCHII regions compared with the previous sources can be due to the beginning of the destruction of such molecules by electronic recombination (Yu & Xu 2016).

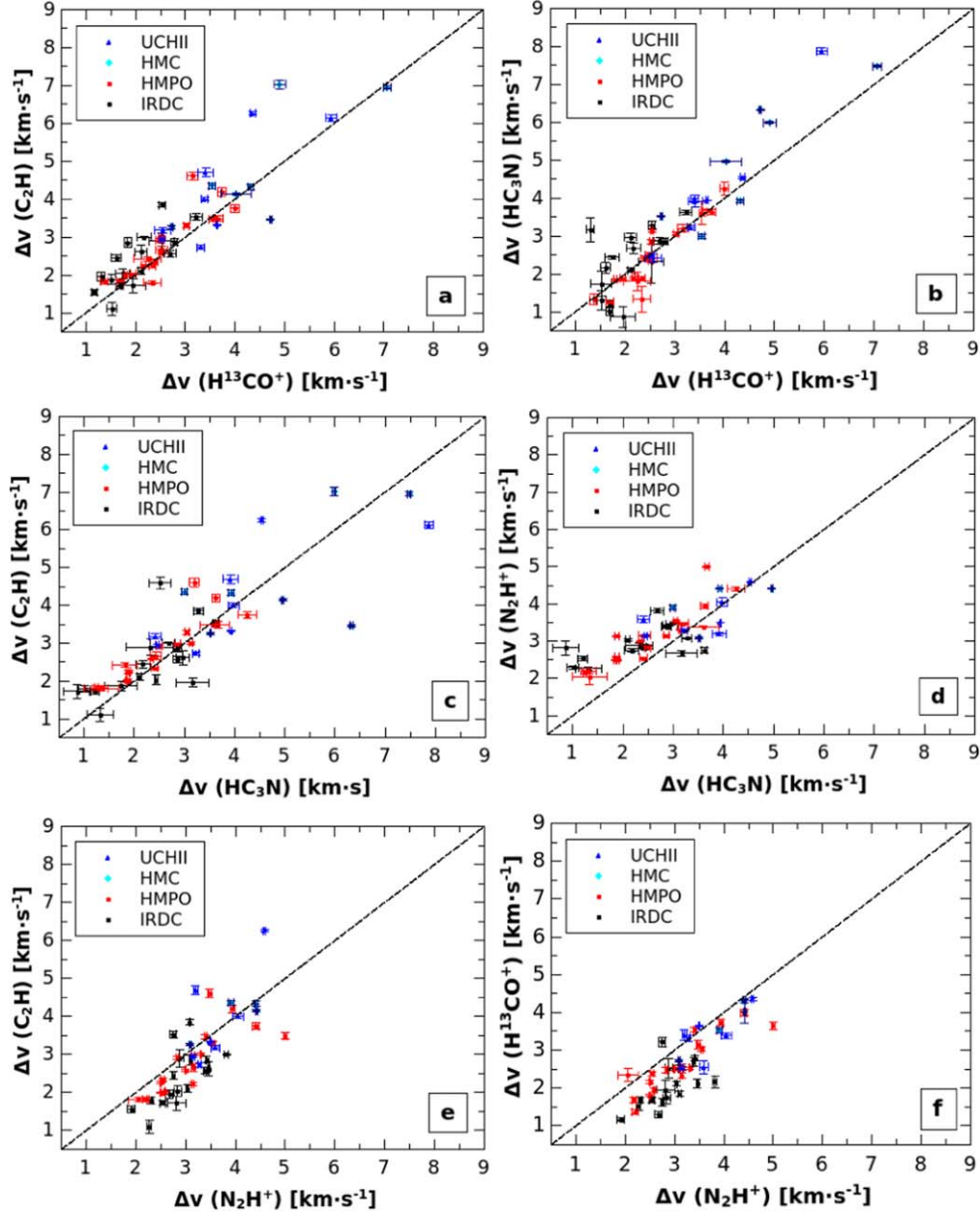


**Figure 4.** Plots of the FWHM line widths ( $\Delta v$ ) obtained from Gaussian fittings to the emission lines of  $C_2H$ ,  $H^{13}CO^+$ ,  $HC_3N$  and  $N_2H^+$ . The dashed black lines indicate unity. Error bars represent the formal errors of the Gaussian fittings.

It is worth noting that the discussed behavior in the column densities (which have molecular excitation assumptions) regarding the correlation with the evolutionary stage from IRDCs to HMCs is quite similar to the comparison between the integrated intensities and the peak submillimeter flux (which are direct measurements). Thus, in the line of a chemical clock analysis, even though more statistics are necessary, we propose that these relations, mainly the  $N(N_2H^+)$  versus  $N(H^{13}CO^+)$  and the  $I(C_2H)$  versus  $F_{870\ \mu m}$ , in which the different kinds of

sources (IRDCs, HMPOs and HMCs) are clearly separated, could be used to differentiate them, which can be useful in works handling a large amount of sources of unknown, or not completely known, nature.

The comparison between the relative abundance ratios  $[C_2H]/[H^{13}CO^+]$  versus  $[N_2H^+]/[H^{13}CO^+]$  (Figure 6) presents a high dispersion, mainly along the y-axis, i.e., in the  $N(C_2H)/N(H^{13}CO^+)$  ratio, and does not show a remarkable difference as it was found between MYSOs and H II regions by

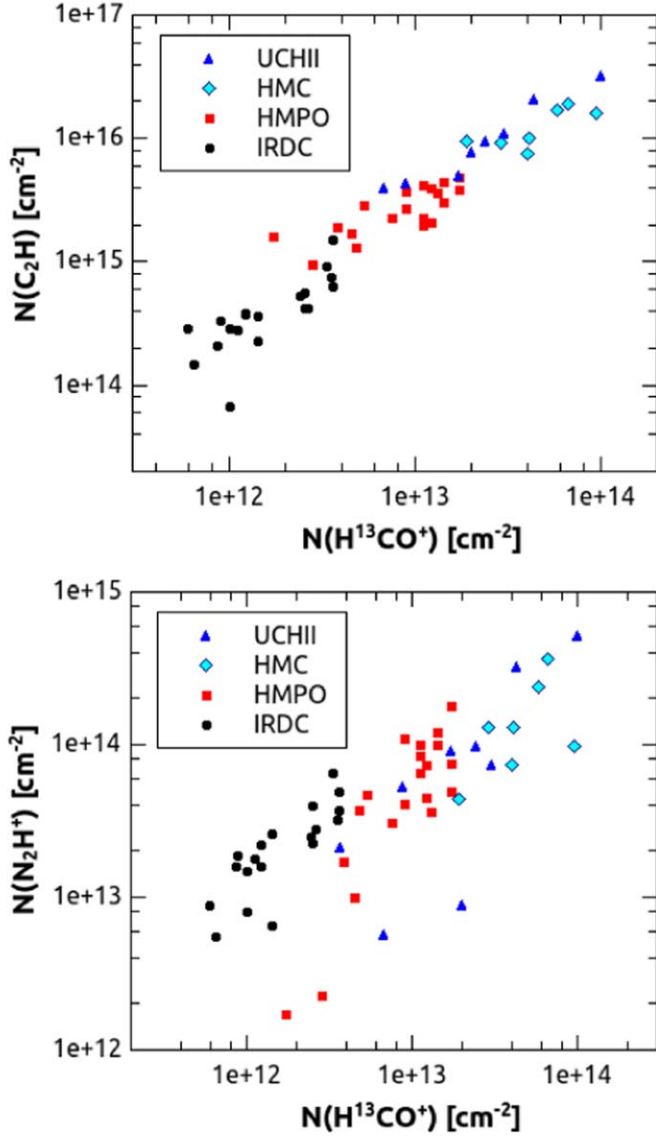


**Figure 5.** Column densities of  $C_2H$  (top) and  $N_2H^+$  (bottom) against column density of  $H^{13}CO^+$ . The column density values were obtained from Gerner et al. (2014).

Yu & Wang (2015). However, along the  $x$ -axis, i.e., in the  $N(N_2H^+)/N(H^{13}CO^+)$  ratio, some trend can be appreciated, mainly such a ratio seems to be larger in IRDCs in comparison with the other kind of sources, which in the line of a chemical clock analysis, we suggest that this abundance ratio can be used to differentiate the earliest stage of the star-forming regions.

The molecular line widths (FWHM) are usually associated with the kinematics of the molecular gas and can be affected by multiple events, such as shocks, outflows, rotation of the clump and turbulence. In this work, we assume that line widths originate mainly from the increasing turbulence that arises as a consequence of evolving star formation stages (Sanhueza et al.

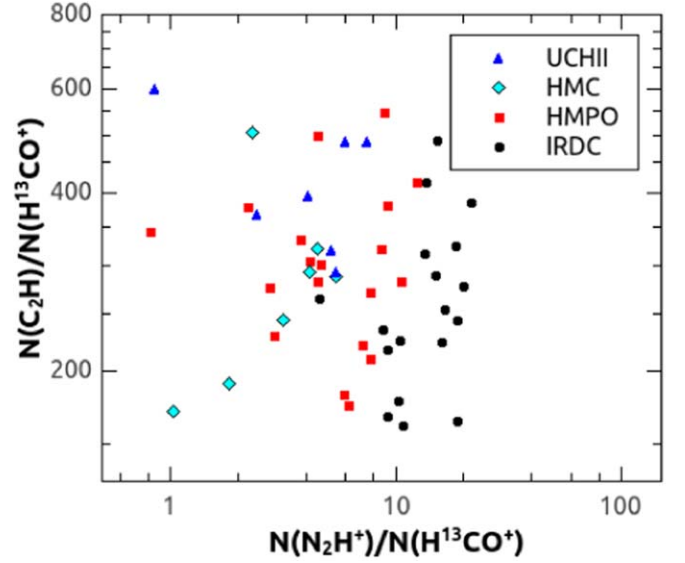


**Figure 6.** Relative abundance of  $[C_2H]/[H^{13}CO^+]$  versus  $[N_2H^+]/[H^{13}CO^+]$ . The column density values were obtained from Gerner et al. (2014).

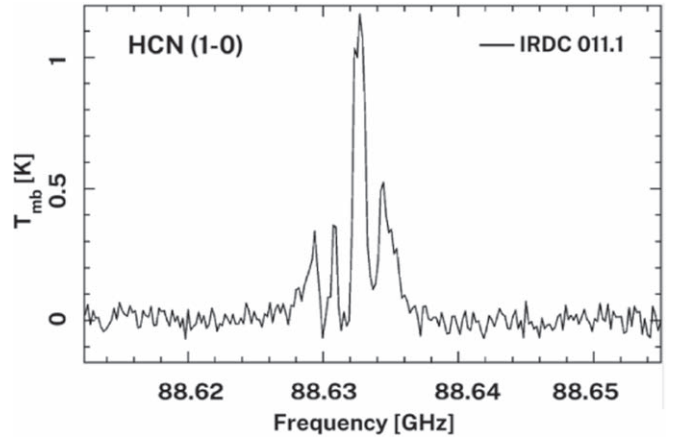


**Figure 7.** Example of an HCN spectrum with strong signatures of saturation which affects the use of the HCN–HNC ratio as a thermometer yielding unreliable temperatures below 15 K.

2012; Yu & Wang 2015). With this in mind, by analyzing the average line width of  $N_2H^+$ ,  $HC_3N$ ,  $H^{13}CO^+$  and  $C_2H$  (see Table 7), it can be appreciated that in the four species, the line width rises until reaching the HMC stage. Such an increase could be a consequence of the gas dynamics related to the star-forming processes that take place in the molecular clumps (Fontani et al. 2002; Pirogov et al. 2003). Particularly, our  $\Delta\nu(N_2H^+)$  average values are in quite good agreement with those presented by Sanhueza et al. (2012): the  $\Delta\nu(N_2H^+)$  average value that we obtained for IRDCs is similar to that obtained by the authors in their so-called “quiescent” and “intermediate” clumps, while the value that we obtained for



HMPOs is in agreement with the values of their “active” clumps. Finally, our  $\Delta v(\text{N}_2\text{H}^+)$  average values obtained for HMCs and UCHII regions are slightly larger than the value obtained for their “red” clumps. Following Sanhueza et al. (2012), we can confirm that line widths of  $\text{N}_2\text{H}^+$  slightly increase with the evolution of the clumps.

As found by Sanhueza et al. (2012) in their sample of clumps embedded in IRDCs, we observed that in our sources, the  $\text{H}^{13}\text{CO}^+$  and  $\text{HC}_3\text{N}$  have slightly narrower line widths than  $\text{N}_2\text{H}^+$  (see panels d and f in Figure 4). This hints that they trace similar optically thin gas emanating from the internal layers of the regions, and according to our findings, it seems to be independent of the kind of source. Yu & Wang (2015) found that the best  $\Delta v$  correlation is between  $\text{C}_2\text{H}$  and  $\text{N}_2\text{H}^+$  for their sample of EGOs. In our case, we did not find such a good correlation between these molecular species (see panel e in Figure 4). The  $\text{C}_2\text{H}$  line widths are slightly narrower than those of the  $\text{N}_2\text{H}^+$ . Sanhueza et al. (2012) also remarked that the  $\text{C}_2\text{H}$  appears to present the best correlation with  $\text{N}_2\text{H}^+$  among all the studied  $\Delta v$  relations. However, by inspecting their  $\Delta v(\text{C}_2\text{H})$  versus  $\Delta v(\text{N}_2\text{H}^+)$  plot, we observe a similar behavior as our plot, where most of the points tend to be below the unity line.

In the spectra of these four molecular species toward the whole sample, we did not find line wings that may probe outflows, except for the  $\text{HC}_3\text{N}$  spectra of HMPO18247, HMC029.96 (see Figure A6) and UCH10.30, and in the  $\text{H}^{13}\text{CO}^+$  spectrum of HMC34.26, in which small spectral wings appear. UCH10.30 is an EGO; the other sources present  $4.5\ \mu\text{m}$  extended emission and diffuse emission at the Ks band. Besides these sources, it can be noticed that the near-infrared (near-IR) evidence of jets or/and outflows does not have any direct correlation with spectral features in the emission of  $\text{N}_2\text{H}^+$ ,  $\text{HC}_3\text{N}$ ,  $\text{H}^{13}\text{CO}^+$  or  $\text{C}_2\text{H}$ .

## 5. Summary and Concluding Remark

We presented a spectroscopic molecular line analysis of 55 high-mass star-forming regions with the aim of probing some chemical tools that were recently proposed to characterize such regions. The analyzed sources are classified as IRDCs, HMPOs, HMCs and UCHII regions, according to an evolutionary progression in the high-mass star formation. The main results can be summarized as follows:

1. The emissions of the HCN and HNC isomers were used to estimate the kinetic temperature through a new “thermometer” whose formulation was proposed by Hacar et al. (2020), and we investigated its use in the presented sample of sources. By comparing the  $T_K$  derived from the HCN/HNC ratio with temperatures obtained from the dust and ammonia emission, we found that the use of such a ratio as a universal thermometer in the ISM should be taken with care. The HCN optical depth is a big issue to be taken into account. Line saturation may explain the derived temperature values below 15 K, which must be

discarded, and mainly correspond to IRDCs and HMPOs. In addition, we found that, although the  $T_K$  obtained from the HCN–HNC tool is greater than 15 K, its value could be far from the temperatures obtained from the dust or ammonia, yielding lower temperatures. This is the case of HMCs and UCHII regions of our sample, in which, in general, it is observed that the HCN hyperfine line  $F=1-1$  appears absorbed. In conclusion, we point out that the HCN–HNC tool as a kinetic temperature estimator should be used only after a careful analysis of the HCN spectrum, checking that no line, either the main or the hyperfine ones, presents absorption features.

2. Additionally, we analyzed the molecular species  $\text{N}_2\text{H}^+$ ,  $\text{HC}_3\text{N}$ ,  $\text{H}^{13}\text{CO}^+$  and  $\text{C}_2\text{H}$  in the sample of sources focusing on the use of them as “chemical clocks.” The comparison of the molecular integrated intensities of  $\text{HC}_3\text{N}$ ,  $\text{N}_2\text{H}^+$ ,  $\text{C}_2\text{H}$  and also of HNC with the  $870\ \mu\text{m}$  peak flux, as well as the relations of the column densities of  $\text{C}_2\text{H}$  and  $\text{N}_2\text{H}^+$  with that of the  $\text{H}^{13}\text{CO}^+$ , can be useful to distinguish regions among IRDCs, HMPOs and HMCs, which complement the Yu & Wang (2015) results. On the other hand, from the  $[\text{C}_2\text{H}]/[\text{H}^{13}\text{CO}^+]$  versus  $[\text{N}_2\text{H}^+]/[\text{H}^{13}\text{CO}^+]$  relation, we can point out that even though the  $[\text{C}_2\text{H}]/[\text{H}^{13}\text{CO}^+]$  ratio shows a large dispersion along the analyzed sources, the  $[\text{N}_2\text{H}^+]/[\text{H}^{13}\text{CO}^+]$  ratio seems to be larger in IRDCs in comparison with the other kind of sources analyzed in this work. Finally, regarding the molecular line widths, we found that the  $\Delta v$  rises from the IRDC to the HMC stage, which could be due to the increasing turbulence as a consequence of the evolution of the star-forming processes.

In conclusion, this work explores chemical tools, some of them based on direct measurements, to be applied in different ISM environments. In that sense, we probed such tools in a new sample of sources with respect to previous works, and these results not only contribute to more statistics in the literature but also complement such works with other types of sources. Using direct tools, like, for instance, the ratios of different molecular parameters that can be directly measured from the observations, can be very useful mainly when a large sample of sources is handled. If it is proven that such tools are reliable, they can be used to obtain important statistical information in a simple way. Our work points to it and encourages performing similar works in larger samples of sources of different types.

## Acknowledgments

We thank the anonymous referee for her/his useful comments that improved our work. N.C.M. is a doctoral fellow of CONICET, Argentina. S.P. is a member of the *Carrera del Investigador Científico* of CONICET, Argentina. This work was partially supported by the Argentina grants PIP 2021 11220200100012 and PICT 2021-GRF-TII-00061 awarded by CONICET and ANPCYT.

### Appendix Example Spectra

In this appendix we include some spectra of the analyzed molecular lines as an example of each kind of source, showing the integrated area in the case of the HCN and HNC emissions

and the Gaussian fittings for the  $\text{H}^{13}\text{CO}^+$ ,  $\text{C}_2\text{H}$ ,  $\text{HC}_3\text{N}$  and  $\text{N}_2\text{H}^+$ . Spectra of IRDC18151 are shown in Figures A1 and A2, of HMPO20126 in Figures A3 and A4, of HMC0.29.26 in Figures A5 and A6, and of UCHII 45.45 in Figures A7 and A8.

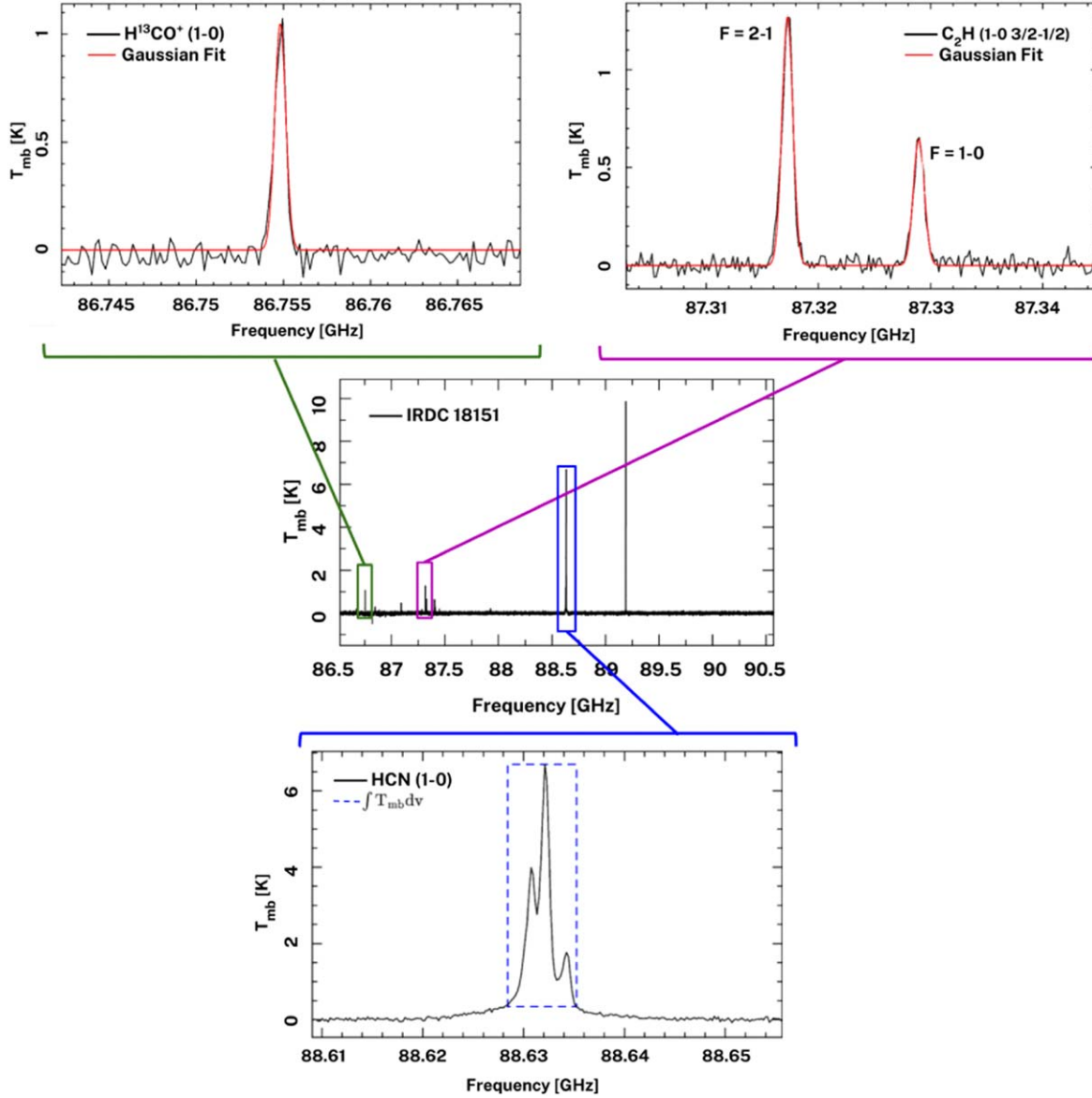


**Figure A1.** IRAM spectra containing the HCN,  $\text{H}^{13}\text{CO}^+$  and  $\text{C}_2\text{H}$  lines toward IRDC18151. The integrated area in the HCN emission and the Gaussian fittings for the other molecular lines are shown.

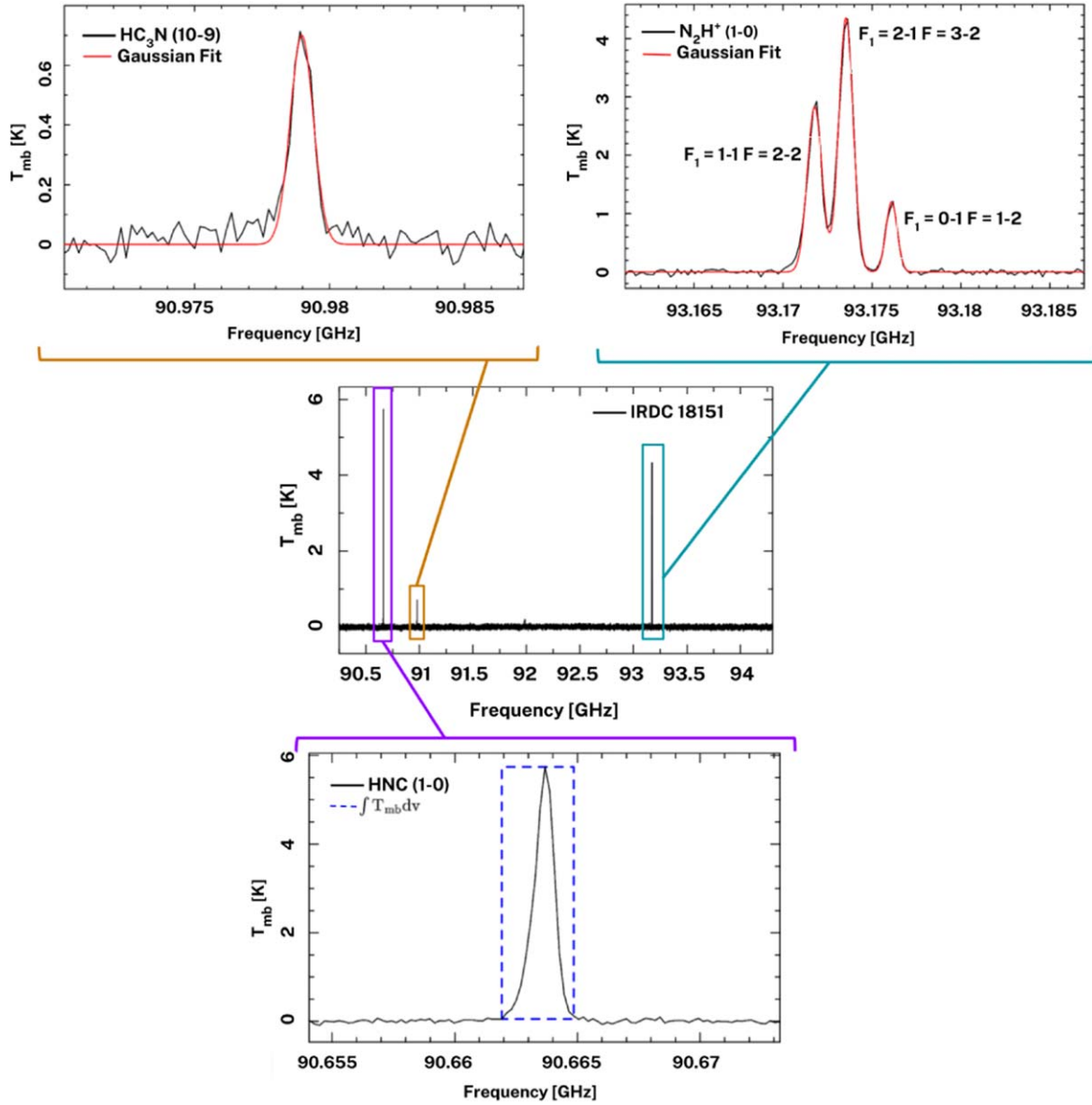


**Figure A2.** IRAM spectra containing the HNC,  $\text{HC}_3\text{N}$  and  $\text{N}_2\text{H}^+$  lines toward IRDC18151. The integrated area in the HNC emission and the Gaussian fittings for the other molecular lines are shown.

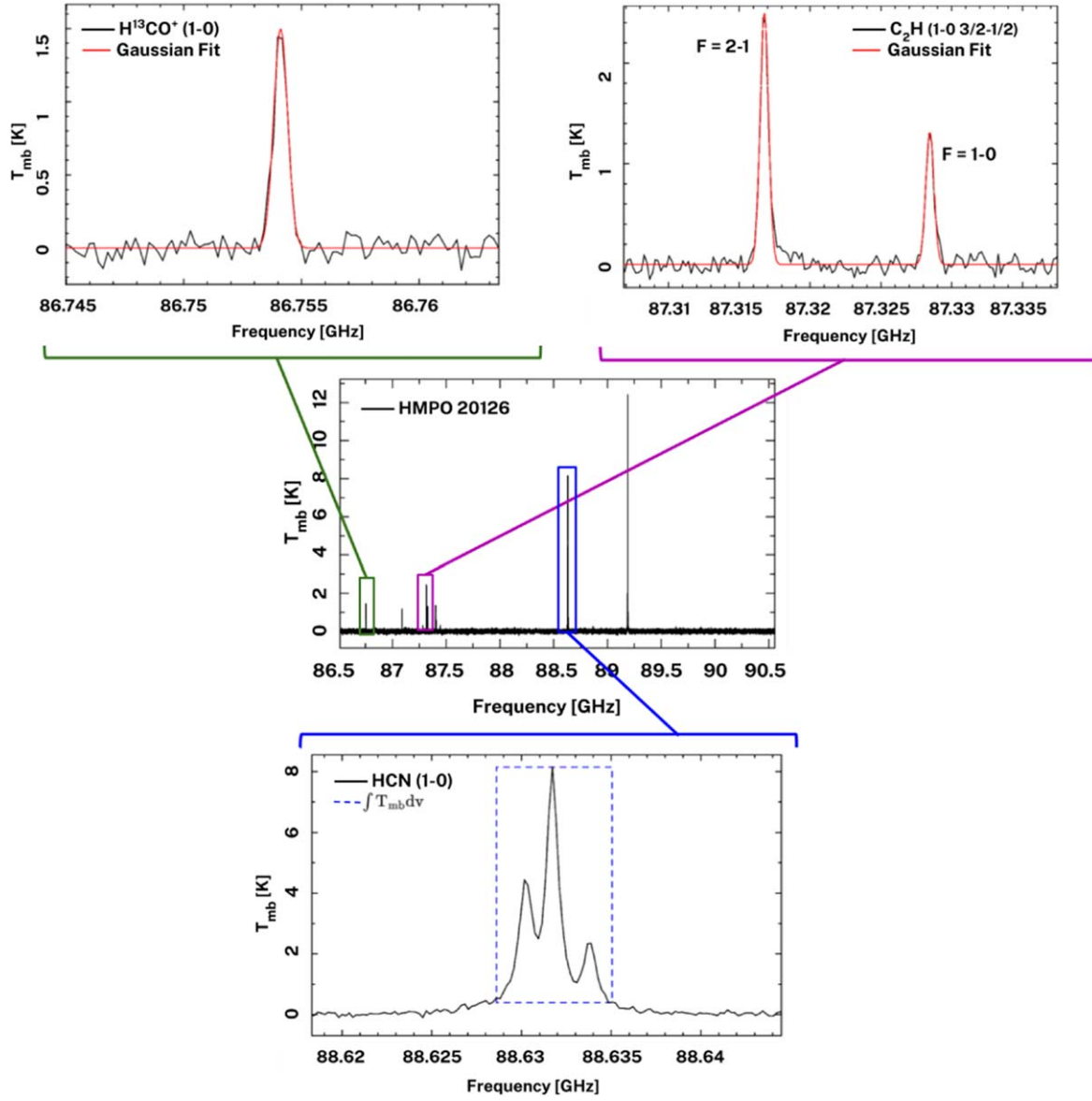


**Figure A3.** IRAM spectra containing the HCN,  $\text{H}^{13}\text{CO}^+$  and  $\text{C}_2\text{H}$  lines toward HMPO20126. The integrated area in the HCN emission and the Gaussian fittings for the other molecular lines are shown.

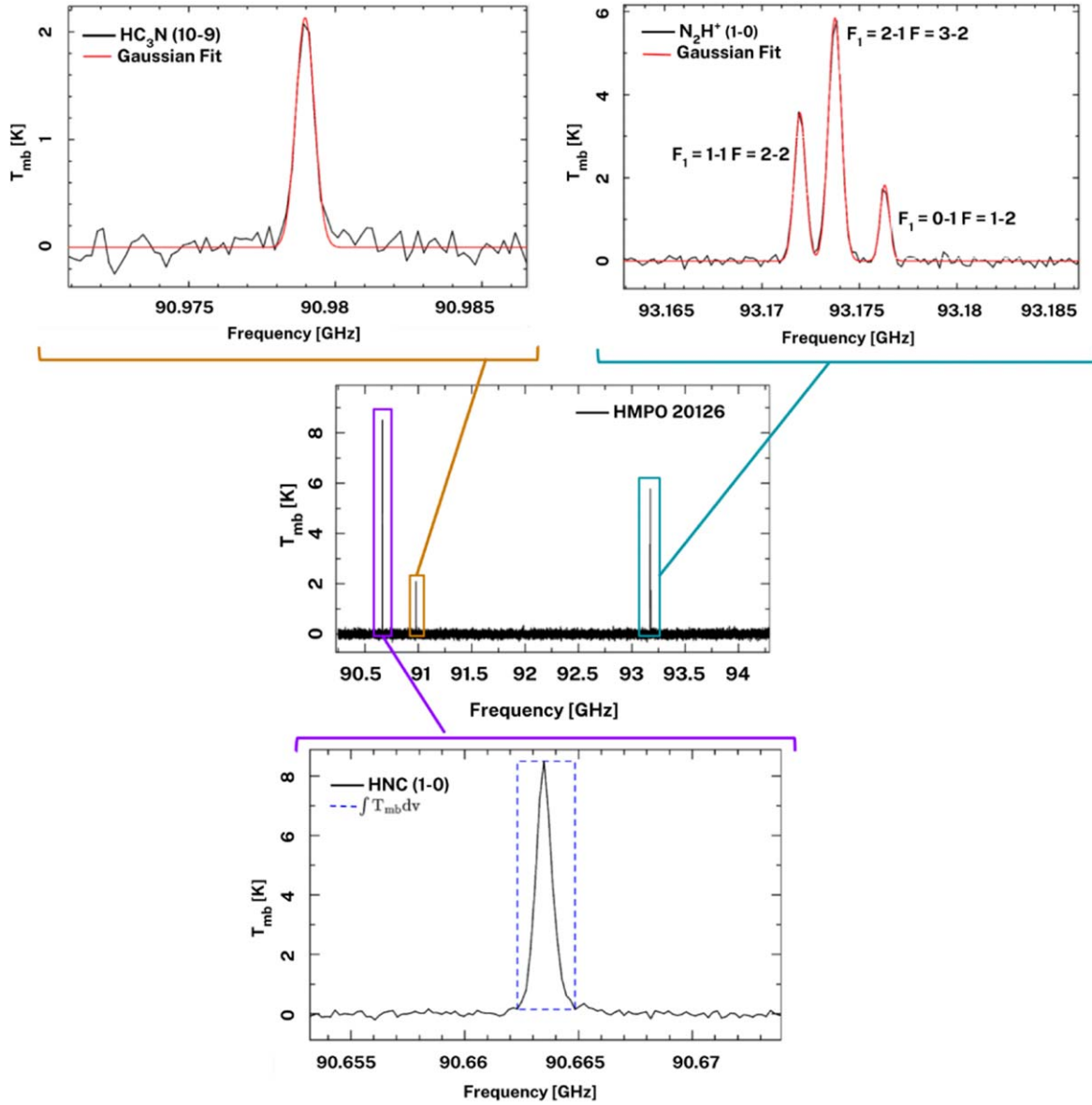


**Figure A4.** IRAM spectra containing the HNC,  $\text{HC}_3\text{N}$  and  $\text{N}_2\text{H}^+$  lines toward HMPO20126. The integrated area in the HNC emission and the Gaussian fittings for the other molecular lines are shown.



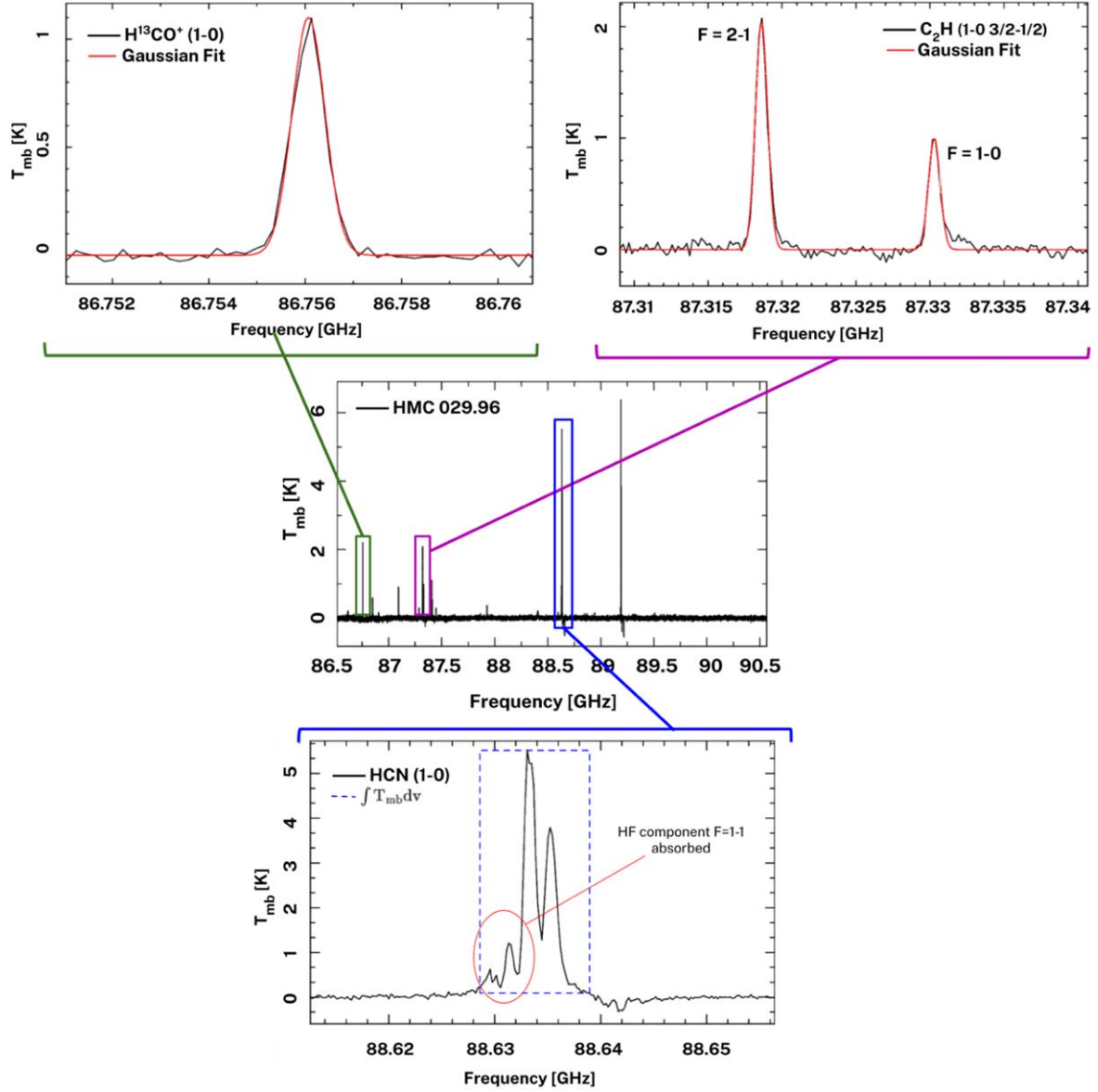


**Figure A5.** IRAM spectra containing the  $\text{HCN}$ ,  $\text{H}^{13}\text{CO}^+$  and  $\text{C}_2\text{H}$  lines toward HMC029.96. The integrated area in the  $\text{HCN}$  emission and the Gaussian fittings for the other molecular lines are shown. In the case of  $\text{HCN}$  it is remarked that the hyperfine component  $F = 1-1$  is absorbed.

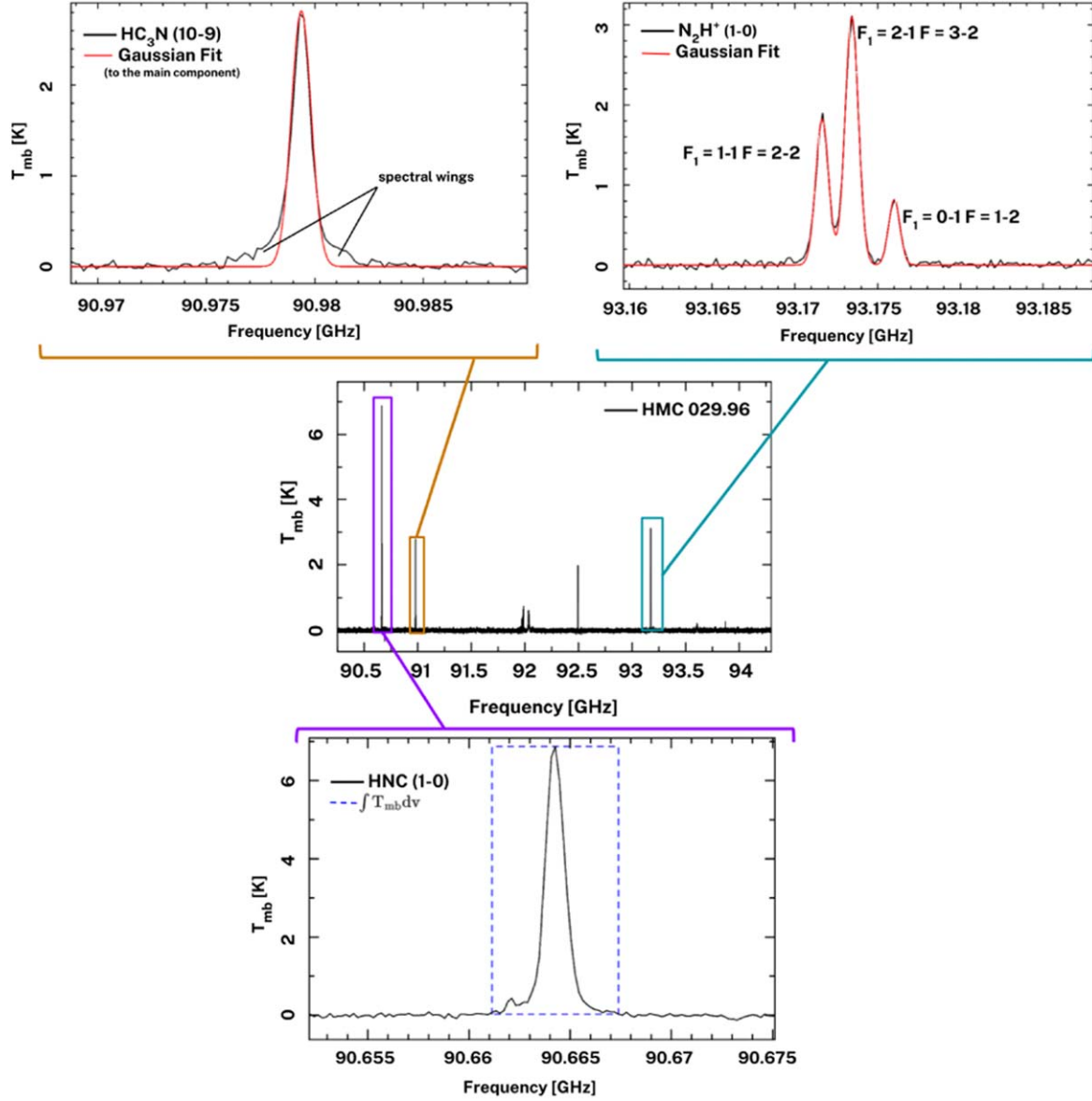


**Figure A6.** IRAM spectra containing the HNC,  $\text{HC}_3\text{N}$  and  $\text{N}_2\text{H}^+$  lines toward HMC029.96. The integrated area in the HNC emission and the Gaussian fittings for the other molecular lines are shown. In the case of the  $\text{HC}_3\text{N}$  emission small spectral wings appear, and the Gaussian fitting corresponds to the main component.

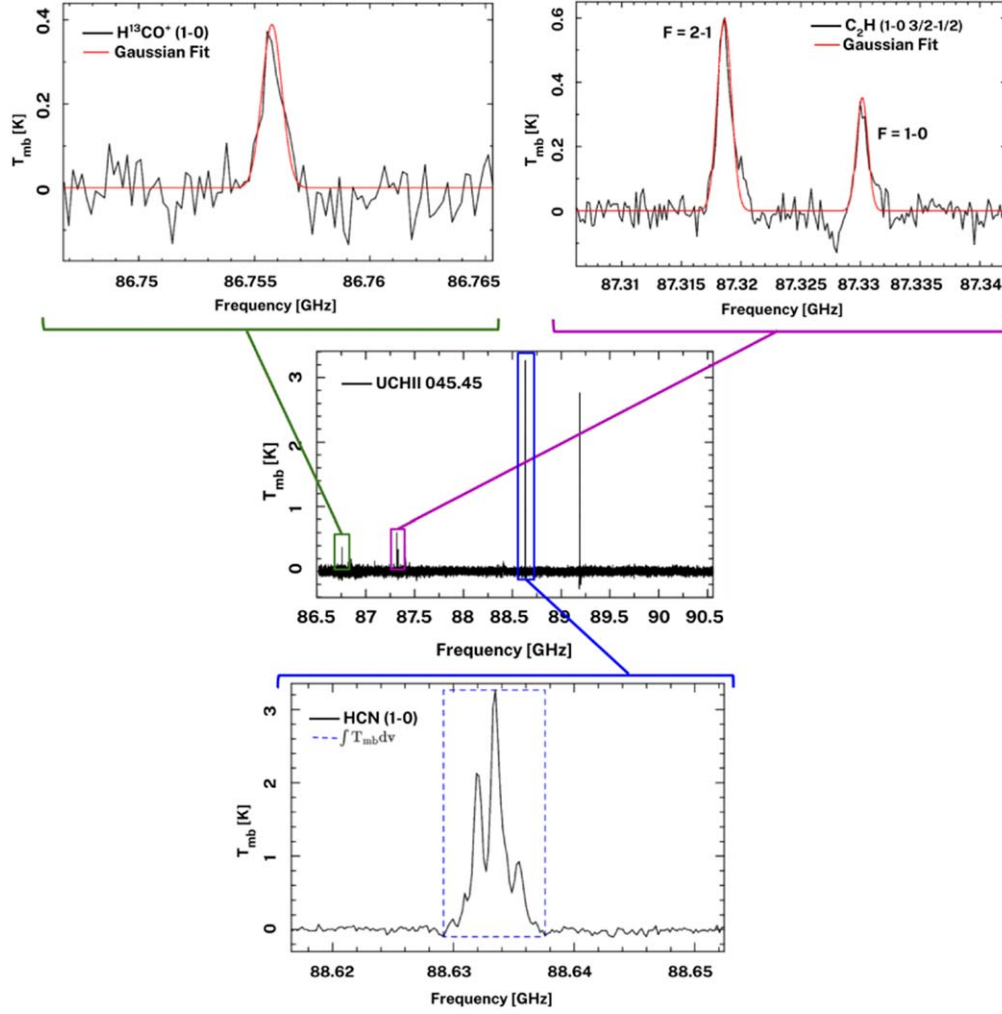


**Figure A7.** IRAM spectra containing the  $\text{HCN}$ ,  $\text{H}^{13}\text{CO}^+$  and  $\text{C}_2\text{H}$  lines toward UCHII 45.45. The integrated area in the  $\text{HCN}$  emission and the Gaussian fittings for the other molecular lines are shown.

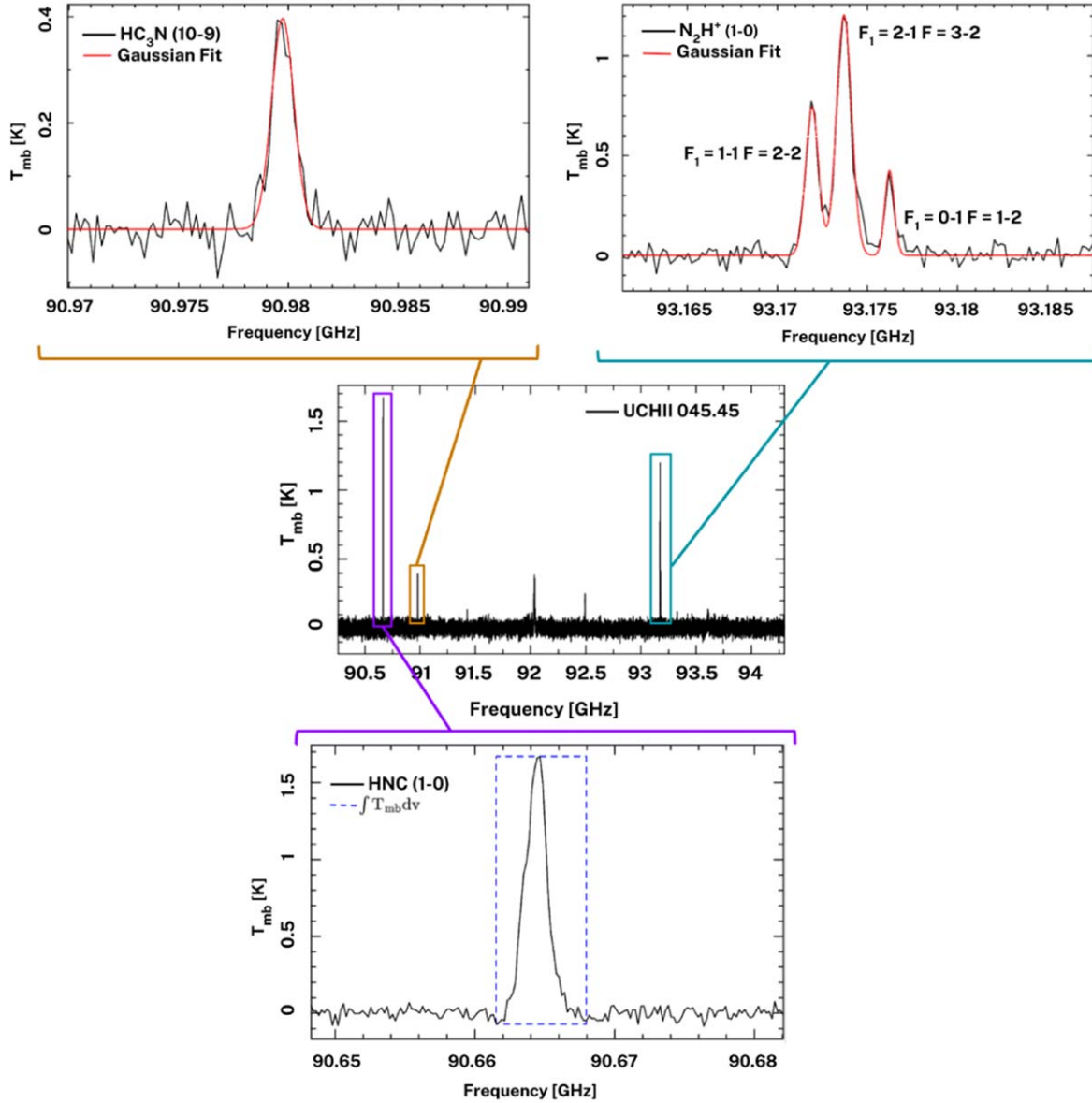


**Figure A8.** IRAM spectra containing the HNC, HC<sub>3</sub>N and N<sub>2</sub>H<sup>+</sup> lines toward UCHII 45.45. The integrated area in the HNC emission and the Gaussian fittings for the other molecular lines are shown.

## References

- Bergin, E. A., Goldsmith, P. F., Snell, R. L., & Langer, W. D. 1997, *ApJ*, **482**, 285
- Bergin, E. A., Snell, R. L., & Goldsmith, P. F. 1996, *ApJ*, **460**, 343
- Betz, A. L., McLaren, R. A., & Spears, D. L. 1979, *ApJL*, **229**, L97
- Beuther, H., Churchwell, E. B., McKee, C. F., & Tan, J. C. 2007, in *Protostars and Planets V*, ed. B. Reipurth, D. Jewitt, & K. Keil (Tucson: Univ. Arizona Press), 165
- Beuther, H., Semenov, D., Henning, T., & Linz, H. 2008, *ApJL*, **675**, L33
- Bögnér, R., Csengeri, T., Montillaud, J., et al. 2022, *A&A*, **667**, A137
- Bonfand, M., Belloche, A., Garrod, R. T., et al. 2019, *A&A*, **628**, A27
- Churchwell, E., Babler, B. L., Meade, M. R., et al. 2009, *PASP*, **121**, 213
- Contreras, Y., Schuller, F., Urquhart, J. S., et al. 2013, *A&A*, **549**, A45
- Cyganowski, C. J., Whitney, B. A., Holden, E., et al. 2008, *AJ*, **136**, 2391
- Davis, C. J., Kumar, M. S. N., Sandell, G., et al. 2007, *MNRAS*, **374**, 29
- Duronea, N. U., Bronfman, L., Mendoza, E., et al. 2019, *MNRAS*, **489**, 1519
- Fontani, F., Cesaroni, R., Caselli, P., & Olmi, L. 2002, *A&A*, **389**, 603
- Foster, J. B., Jackson, J. M., Barnes, P. J., et al. 2011, *ApJS*, **197**, 25
- Fuente, A., Martín-Pintado, J., Cernicharo, J., & Bachiller, R. 1993, *A&A*, **276**, 473
- García-Burillo, S., Viti, S., Combes, F., et al. 2017, *A&A*, **608**, A56
- Gerner, T., Beuther, H., Semenov, D., et al. 2014, *A&A*, **563**, A97
- Giannetti, A., Leurini, S., Wyrowski, F., et al. 2017, *A&A*, **603**, A33
- Guzmán, A. E., Sanhueza, P., Contreras, Y., et al. 2015, *ApJ*, **815**, 130
- Hacar, A., Bosman, A. D., & van Dishoeck, E. F. 2020, *A&A*, **635**, A4
- Herbst, E., & van Dishoeck, E. F. 2009, *ARA&A*, **47**, 427

- Ho, P. T. P., & Barrett, A. H. 1980, in *Interstellar Molecules*, ed. B. H. Andrew, Vol. 87 (Dordrecht: D. Reidel Publishing Co.), 175
- Ho, P. T. P., & Townes, C. H. 1983, *ARA&A*, 21, 239
- Hoare, M. G., Lumsden, S. L., Oudmaijer, R. D., et al. 2005, in *Massive Star Birth: A Crossroads of Astrophysics*, ed. R. Cesaroni et al., Vol. 227 (Cambridge: Cambridge Univ. Press), 370
- Jackson, J. M., Rathborne, J. M., Foster, J. B., et al. 2013, *PASA*, 30, e057
- Jørgensen, J. K., Belloche, A., & Garrod, R. T. 2020, *ARA&A*, 58, 727
- Jørgensen, J. K., Schöier, F. L., & van Dishoeck, E. F. 2004, *A&A*, 416, 603
- Lawrence, A., Warren, S. J., Almaini, O., et al. 2007, *MNRAS*, 379, 1599
- Li, M., Zhou, J., Esimbek, J., et al. 2019, *ApJS*, 243, 13
- Loughnane, R. M., Redman, M. P., Thompson, M. A., et al. 2012, *MNRAS*, 420, 1367
- Marsh, K. A., Whitworth, A. P., & Lomax, O. 2015, *MNRAS*, 454, 4282
- Marsh, K. A., Whitworth, A. P., Lomax, O., et al. 2017, *MNRAS*, 471, 2730
- Martin, R. N., & Ho, P. T. P. 1979, *A&A*, 74, L7
- Motte, F., Bontemps, S., & Louvet, F. 2018, *ARA&A*, 56, 41
- Mottram, J. C., Urquhart, J. S., Hoare, M. G., Lumsden, S. L., & Oudmaijer, R. D. 2006, arXiv:astro-ph/0612481
- Nagy, Z., Ossenkopf, V., Van der Tak, F. F. S., et al. 2015, *A&A*, 578, A124
- Nomura, H., & Millar, T. J. 2004, *A&A*, 414, 409
- Paron, S., Mast, D., Fariña, C., et al. 2022, *A&A*, 666, A105
- Pirogov, L., Zinchenko, I., Caselli, P., Johansson, L. E. B., & Myers, P. C. 2003, *A&A*, 405, 639
- Rathborne, J. M., Lada, C. J., Muench, A. A., Alves, J. F., & Lombardi, M. 2008, *ApJS*, 174, 396
- Rawlings, J. M. C., Redman, M. P., Keto, E., & Williams, D. A. 2004, *MNRAS*, 351, 1054
- Sanhueza, P., Jackson, J. M., Foster, J. B., et al. 2012, *ApJ*, 756, 60
- Sanhueza, P., Jackson, J. M., Foster, J. B., et al. 2013, *ApJ*, 773, 123
- Schilke, P., Walmsley, C. M., Pineau Des Forets, G., et al. 1992, *A&A*, 256, 595
- Snyder, L. E., & Buhl, D. 1971, *ApJL*, 163, L47
- Snyder, L. E., & Buhl, D. 1972, *NYASA*, 194, 17
- Stephens, I. W., Jackson, J. M., Sanhueza, P., et al. 2015, *ApJ*, 802, 6
- Takano, S., Takano, T., Nakai, N., Kawaguchi, K., & Schilke, P. 2013, *A&A*, 552, A34
- Tan, J. C., Beltrán, M. T., Caselli, P., et al. 2014, in *Protostars and Planets VI*, ed. H. Beuther et al. (Tucson: Univ. Arizona Press), 149
- Taniguchi, K., Saito, M., & Ozeke, H. 2016, *ApJ*, 830, 106
- Urquhart, J. S., Figura, C., Wyrowski, F., et al. 2019, *MNRAS*, 484, 4444
- Urquhart, J. S., Hoare, M. G., Lumsden, S. L., Oudmaijer, R. D., & Moore, T. J. T. 2008, in *ASP Conf. Ser. 387, Massive Star Formation: Observations Confront Theory*, ed. H. Beuther, H. Linz, & T. Henning (San Francisco, CA: ASP), 381
- Urquhart, J. S., Moore, T. J. T., Csengeri, T., et al. 2014, *MNRAS*, 443, 1555
- Urquhart, J. S., Morgan, L. K., Figura, C. C., et al. 2011, *MNRAS*, 418, 1689
- Veena, V. S., Vig, S., Mookerjee, B., et al. 2018, *ApJ*, 852, 93
- Vigren, E., Zhaunerchyk, V., Hamberg, M., et al. 2012, *ApJ*, 757, 34
- Walmsley, C. M., Churchwell, E., Nash, A., & Fitzpatrick, E. 1982, *ApJL*, 258, L75
- Yu, N., & Wang, J.-J. 2015, *MNRAS*, 451, 2507
- Yu, N., & Xu, J. 2016, *ApJ*, 833, 248
- Zinnecker, H., & Yorke, H. W. 2007, *ARA&A*, 45, 481